

UNIVERSIDADE DE SÃO PAULO
INSTITUTO DE FÍSICA DE SÃO CARLOS

GUSTAVO FORESTO BRITO DE ALMEIDA

Femtosecond laser writing of nonlinear waveguides in Gorilla® Glass
and L-threonine organic crystals

São Carlos
2018

GUSTAVO FORESTO BRITO DE ALMEIDA

Femtosecond laser writing of nonlinear waveguides in Gorilla® Glass
and L-threonine organic crystals

Thesis presented to the Graduate Program
in Physics at the Instituto de Física de São
Carlos, Universidade de São Paulo to
obtain the degree of Doctor of Science.

Concentration area: Basic Physics

Advisor:
Prof. Dr. Cleber Renato Mendonça

Corrected Version

(Original version available on the Program Unit)

São Carlos
2018

I AUTHORIZE THE REPRODUCTION AND DISSEMINATION OF TOTAL OR PARTIAL COPIES OF THIS DOCUMENT, BY CONVENCIONAL OR ELECTRONIC MEDIA FOR STUDY OR RESEARCH PURPOSE, SINCE IT IS REFERENCED.

Almeida, Gustavo Foresto Brito de
Femtosecond laser writing of nonlinear waveguides in
Gorilla® Glass and L-threonine organic crystals / Gustavo
Foresto Brito de Almeida; advisor Cleber Renato Mendonça -
revised version -- São Carlos 2018.
100 p.

Thesis (Doctorate - Graduate Program in Física Básica) -
- Instituto de Física de São Carlos, Universidade de São
Paulo - Brasil , 2018.

1. Femtosecond laser. 2. Nonlinear optics. 3.
Waveguide. 4. Gorilla Glass. 5. Amino acid crystal. I.
Mendonça, Cleber Renato, advisor. II. Title.

Dedicated
to my beloved parents,
Diva and Lauro.

ACKNOWLEDGEMENTS

The realization of this dissertation was only possible due to the collaboration of several people, to which I desire to express my gratitude.

First and foremost, I would like to thank my advisor Prof. Dr. Cleber Renato Mendonça for all his efforts to make me achieve my goals. He is a true advisor that teaches by example with his work ethic, discipline, dedication, passion and excellence. I am thankful for his kindness, patience, friendship and support throughout these years. From day one, his door was always open whenever I needed help with anything. I am fortunate to have had the opportunity to absorb his experiences, and knowledge and I still have a lot to learn from him.

I wish to thank Prof. Dr. José Joatan Rodrigues Jr. from Federal University of Sergipe for the help and for growing many L-threonine crystals that were of extreme relevance for this dissertation.

I would like to thank Prof. Dr. Leonardo De Boni and Prof. Dr. Lino Misoguti for interesting conversations about physics. And also, to Dr. Jonathas Siqueira de Paula for willingly sharing his knowledge on optics and laser.

My sincere thanks to my friends and colleagues from Photonics Group for the valuable discussions and for sharing experiences: Renato Martins, Adriano Otuka, José Francisco Domenegueti, Emerson Barbano, Oriana Avlia, Jessica Dipoldi, Tiago Gualberto, Nathália Tomazio, Luis Felipe Gonçalves (Nó), Ruben Rodriguez, Franciele Henrique, Henry Passagem, Juliana Almeida, Jonathas Siqueira, Sabrina Nicoleti, Kelly Tasso, Leonardo Cocca, Fernando Gotardo, Lucas Sciuti and Flávio Almeida.

Thanks to the Photonics Group staff: Daniel Foschini for the fast and flawless service in the secretary, Dr. Marcos Cardoso for the needed all around support; and André Romero for the countless important helps in experimental setups and friendship.

Thanks to Prof. Craig B. Arnold from Princeton University for giving me the opportunity to work in his laboratory during a summer internship, allowing me to enrich my academic experience in such a prestigious place and for introducing me to Gorilla

Glass. For sure, the great time I had in Princeton was because my friend Juliana Almeida was kind enough to show me the city, the university and to make sure that I felt comfortable away from home. Thank you very much, Ju.

I wish to thank my friends Ernani Jay Vidal, Leonardo Machado, Ramon Rosa, Rafael Souza, Bruno Kemmer and many others from the basketball games.

A very special thanks to my girlfriend Nathália Beretta Tomazio for being with me every day, inside and outside the laboratory. I am glad to have her by my side to support me through the toughest moments and share with me the happiest ones. I simply could not have wished for a more loving and special woman to share my life with.

I would like to express my deep gratitude to my parents, Diva and Lauro, for providing me with endless love, support and encouragement. They are my biggest fans and my greatest heroes. My accomplishments would not have been possible without them. Mom and Dad: I love you!

Thanks to the São Carlos Institute of Physics, that includes the graduation office, library, optical and mechanical shop.

Finally, I am grateful to Coordination for Improvement of Higher Education Personnel (CAPES) for financial support.

“We are what we repeatedly do.
Excellence, then, is not an act,
but a habit.”

Will Durant (1913-1981)

ABSTRACT

ALMEIDA, G. F. B. **Femtosecond laser writing of nonlinear waveguides in Gorilla® Glass and L-threonine organic crystals**. 2018. 100 p. Thesis (Doctor in Science) - Instituto de Física de São Carlos, Universidade de São Paulo, São Carlos, 2018.

Femtosecond laser inscribed waveguides inside the bulk of materials have shown great relevance for the development of photonic optical circuits. Due to high intensity, long interaction length and strong light confinement, nonlinear optical effects are significant to pulse propagation within the waveguide. Therefore, it is important to search for new and better platforms to host photonic devices, as well as, to analyze its linear and nonlinear optical properties. In this dissertation, we have studied the inscription of nonlinear waveguides in Gorilla Glass (strengthened alkali aluminosilicate glass) and in L-threonine organic crystals. Initially, we studied the nonlinear refractive index of Gorilla Glass, demonstrating that it presents an approximately constant value of $n_2 = (3.3 \pm 0.6) \times 10^{-20} \text{ m}^2/\text{W}$ over the spectral region from 490 nm up to 1.5 μm . Single-mode waveguides written in Gorilla Glass presents propagation losses on the order of $(0.35 \pm 0.01) \text{ dB/mm}$, which is comparable to other waveguides inscribed in silicate glasses. In the nonlinear regime, the guided pulse presented spectral broadening, compatible with the measured n_2 value, and white-light continuum generation. The generation of new frequencies is due to self-phase modulation and stimulated Raman scattering effects, both associated with third-order nonlinearities of Gorilla Glass. In a second part, we inscribed cladding waveguides in L-threonine organic crystal, in order to explore its second-order nonlinearities. After their linear characterization, that revealed propagation losses of $(0.5 \pm 0.1) \text{ dB/mm}$, we obtained guided second harmonic generation in the ultraviolet region. The written waveguide presented a normalized power conversion efficiency of $(10.3 \pm 0.4) \% (\text{MW cm}^2)^{-1}$ and approximately four times higher normalized intensity conversion efficiency than the crystal itself. Such enhancement effect was attributed to the influence of the waveguide dispersion in the phase-matching condition necessary for second harmonic generation. In general, the results presented here expand the knowledge on femtosecond laser writing of waveguide in organic and inorganic materials, and their nonlinear properties, which are relevant for developing photonic devices.

Keywords: Femtosecond laser. Nonlinear optics. Waveguide. Gorilla Glass. Amino acid crystal.

RESUMO

ALMEIDA, G. F. B. **Fabricação de guias de onda não lineares com laser de femtossegundo em Gorilla® Glass e cristais orgânicos de L-treonina.** 2018. 100 p. Tese (Doutorado em Ciências) - Instituto de Física de São Carlos, Universidade de São Paulo, São Carlos, 2018.

Guias de ondas fabricados com pulsos de femtossegundos no volume de materiais são de grande importância para o desenvolvimento de circuitos fotônicos. Devido as altas intensidades, longos comprimentos de interação e forte confinamento, efeitos ópticos não lineares são significativos durante a propagação de pulsos laser em guias de onda. Portanto, é importante buscar novas e melhores plataformas para construir os dispositivos fotônicos, bem como analisar suas propriedades ópticas lineares e não lineares de guiamento. Nesta tese, estudamos a fabricação de guias de onda não lineares em *Gorilla Glass* (vidro aluminossilicato alcalino) e no cristal orgânico de L-treonina. Inicialmente, estudamos o índice de refração não linear do *Gorilla Glass*, demonstrando que este apresenta um valor aproximadamente constante, $n_2 = (3,3 \pm 0,6) \times 10^{-20} \text{ m}^2/\text{W}$, no intervalo espectral de 490 nm até 1,5 μm . Os guias monomodo produzidos no *Gorilla Glass* apresentaram perdas de transmissão da ordem de $(0,35 \pm 0,01) \text{ dB/mm}$, as quais são comparáveis às de outros guias em vidros silicatos já reportados. No regime não linear, o pulso guiado apresentou alargamento espectral compatível com o valor determinado para n_2 , e geração de luz branca. A geração de novas frequências observada se deve aos fenômenos de auto modulação de fase e espalhamento Raman estimulado, ambos associados à não linearidade de terceira ordem do *Gorilla Glass*. Numa segunda etapa, fabricamos guias de onda do tipo casca em cristais orgânicos de L-treonina, afim de explorar sua não linearidade de segunda ordem. Após sua caracterização linear, onde medimos uma perda de guiamento de $(0,5 \pm 0,1) \text{ dB/mm}$, fomos capazes de obter geração de segundo harmônico guiada, na região do ultravioleta. O guia fabricado apresentou uma eficiência normalizada de conversão de potência de $(10,3 \pm 0,4) \% (\text{MW cm}^2)^{-1}$ e eficiência normalizada de conversão de intensidade aproximadamente quatro vezes maior do que a do cristal em si. Tal aumento foi atribuído à influência da dispersão do guia no casamento de fase, necessário para geração de segundo harmônico. De maneira geral, os resultados apresentados aqui expandem o conhecimento de fabricação de guias de

onda com laser de femtossegundos em materiais inorgânicos e orgânicos, bem como de suas propriedades não lineares relevantes para produção de dispositivos.

Palavras-chave: Laser de femtossegundos. Óptica não linear. Guia de onda. Gorilla Glass. Cristal de aminoácido.

LIST OF FIGURES

Figure 2.1 – Phase mismatch influence on the efficiency of second harmonic generation process.....	30
Figure 2.2 – Schematic representation of (a) cavity resonant frequency comb, (b) gain	33
Figure 2.3 – Laser output intensity as a function of time in the mode locking regime with (a) 2, (b) 5, (c) 10, (d) 50 and (e) 100 modes, and the case for (f) 100 modes with random relative phases.	34
Figure 2.4 – Illustration of chirped-pulse amplification technique that makes use of an amplification stage, pulse stretcher and compressor.	35
Figure 2.5 – Schematic illustration of (a) linear and nonlinear absorption classified by the process of (b) multiphoton, (c) tunneling and (d) avalanche ionization.....	37
Figure 2.6 – Pulse fluence as a function of the radial distance with two different peak fluences.	41
Figure 2.7 – Step-index optics fiber illustration, acceptance cone, guided and unguided rays.....	43
Figure 2.8 – Dispersion coefficient D of silica optical fiber as function of the wavelength.	48
Figure 2.9 – Pulse (a) intensity and the (b) induced frequency shift as function of the dislocated time.	51
Figure 2.10 – Spectral broadened pulse via self-phase modulation effect.	52
Figure 2.11 – (a) Self-steepening effect of a propagating optical pulse and (b) the asymmetric spectrum generated via self-phase modulation. In both graphs, the light gray line represents the pulse feature before propagation.	54
Figure 2.12 – Raman gain spectrum for fused silica pumped at 1 μm	55
Figure 3.1 – Schematic of the experimental setup used for the (a) open- and (b) closed-aperture Z-scan and (c) Optical-Kerr Gate measurements.....	58
Figure 3.2 – Illustration of the femtosecond laser writing setup in the transverse configuration.	59
Figure 3.3 – Waveguide characterization coupling setup.	60

Figure 4.1 – Nonlinear refractive index of Gorilla Glass obtained by Z-scan measurements. The dashed line is the average value of 3.3×10^{-20} m^2/W . The left inset shows the absorbance spectrum of Gorilla Glass and the right inset displays the experimental (black dots) and theoretical (gray curve) Z-scan signature trace at 810 nm.	64
Figure 4.2 – OKG signal of Gorilla Glass at (a) 520, (b) 650 and (c) 790 nm.	65
Figure 4.3 – Optical microscopy images from ablated grooves at Gorilla Glass surface using fs-laser pulses centered at 520 nm at scanning speed of $50 \mu\text{m}/\text{s}$ as function of pulse energy.	66
Figure 4.4 – Squared groove radii (r_{th2}) as function of the pulse energy at (a) 520, (b) 650 and (c) 775 nm for scanning speeds of (●) 50, (●) 200 and (○) $400 \mu\text{m}/\text{s}$. The lines correspond to the fitting obtained with the expression given in the text. (b) Threshold energy (E_{th}) as a function of excitation wavelength for each scanning speeds.	67
Figure 4.5 – Microscope images of (a) longitudinal and (b) transversal profiles of waveguides fabricated with pulse energy of 250 nJ and its guided mode intensity distribution obtained for coupling light at (c) 632.8 and (d) 775 nm. Scale bar in each image corresponds to $10 \mu\text{m}$	68
Figure 4.6 – Microscope images of transversal profiles of waveguides fabricated with pulse energies of 1.0 and $5.0 \mu\text{J}$ and its corresponding guided mode intensity distributions, for light at 632.8 and 775 nm. Scale bar in each image corresponds to $10 \mu\text{m}$	69
Figure 4.7 – (a) Determination of the Bessel function parameters (kt and γ) and waveguide core radius from the derivative continuity boundary condition, and (b) experimental radial profile data (black dots) fitted by the core (light gray curve) and cladding (dark gray curve) expressions.	70
Figure 4.8 – (a) 260 nJ input pulses spectrum (gray) and its corresponding spectral broadening after propagation in 15-mm long waveguide. (b) Spectrum of the white-light (black) generated by a $380 \mu\text{J}$ input pulse. The gray line displays the transmission of a filter used to attenuate fundamental pulse spectrum. The inset represents a colored image of the corresponding output guided mode.	72
Figure 5.1 – Illustration of (a) type I, (b) type II and (c) type III configurations of waveguides inscribed in transparent material and its respective transversal profiles.	76
Figure 5.2 – (a) Absorbance spectra of a 1.5 mm-thick L-threonine crystal for light polarized parallel to the principal axes. Curves for y and z axes are vertically shifted. (b) L-threonine refractive index dispersion.	77

Figure 5.3 – Longitudinal (a) and transversal (b) optical microscope images of inscribed waveguide.....	78
Figure 5.4 – Double-line inscribed waveguides (a) longitudinal and (b) transversal optical microscope images, and its (c) guided mode intensity profile at 632.8 nm.....	79
Figure 5.5 – (a) Three-dimensional scheme of the inscribed cladding waveguide and microscope images of its (b) transversal and (c) longitudinal profiles.....	79
Figure 5.6 – fs-laser inscribed cladding waveguide transmission as function of the input numerical aperture lens for cw laser at the wavelengths of (a) 632.8 nm and (b) 800 nm. Its correspondent guided mode intensity distributions for an input NA of 0.1 are shown in the insets.....	80
Figure 5.7 – (a) Guided second harmonic beam power (black squares) and its conversion efficiency (blue circles) as function of the fundamental beam power at the waveguide output. The inset corresponds to the mode intensity distribution of the guided second harmonic. (b) Second harmonic beam power (black squares) and its conversion efficiency (blue circles) as function of the fundamental beam power for the crystal. (c) Spectra of fundamental input (red) and second harmonic output (blue) beams in the crystal (dotted line) and guided within the waveguide (solid line).	82

LIST OF ABBREVIATIONS AND ACRONYMS

BBO	β -Barium Borate
CPA	Chirped-Pulse Amplification
<i>cw</i>	continuous wave
FWHM	Full Width Half Maximum
GDV	Group Velocity Dispersion
KDP	Potassium Dihydrogen Phosphate
KTP	Potassium Titanyl Phosphate
LIPSS	Laser Induced Periodic Surface Structures
MI	Modulation Instability
NA	Numerical Aperture
NIR	Near Infrared
NLSE	Nonlinear Schrödinger Equation
OKG	Optical Kerr-Gate
OPA	Optical Parametric Amplification
OPO	Optical Parametric Oscillation
SCG	Supercontinuum Generation
SPM	Self-Phase Modulation
SHG	Second Harmonic Generation
SRS	Stimulated Raman Scattering
SSFS	Soliton Self-Frequency Shift
SVEA	Slowly Varying Amplitude Approximation
THG	Third Harmonic Generation
UV	Ultra-violet
WLC	White-light Continuum
XPM	Cross-Phase Modulation

LIST OF SYMBOLS

E	electric field
P	polarization
E_g	gap energy
\hbar	Planck constant divided by 2π
ω	frequency
ϕ	phase
k	propagation constant
n	refractive index
c	speed of light in vacuum
χ	electric susceptibility
I	intensity
γ_K	Keldysh parameter
λ	wavelength
α_{dB}	Waveguide attenuation
D	dispersion coefficient
t_0	temporal pulse width
w_0	spot size
β	guided propagation constant
n_2	nonlinear refractive index
L_D	waveguide dispersion length
L_{NL}	waveguide nonlinear length
ϵ_0	vacuum permittivity
A_{eff}	modal effective area
γ	nonlinear coefficient
Δk	phase mismatch
F	fluence
Ω_{tun}	“tuning” frequency
α_{coupl}	coupling losses
J_m	Bessel function of first kind

K_m	Modified Bessel function of first kind
F_{th}	fluence threshold
E_{th}	energy threshold

CONTENTS

1	INTRODUCTION	23
2	THEORETICAL BASIS	27
2.1	Nonlinear optics	27
2.2	Ultrashort pulse generation	32
2.3	Fundamentals of fs-laser material processing	36
2.4	Nonlinear effects in waveguide structure	43
2.4.1	Waveguide structure and pulse propagation.....	43
2.4.2	Self-phase modulation and optical soliton.....	50
2.4.3	Four-wave mixing.....	53
2.4.4	Self-steepening	54
2.4.5	Stimulated Raman scattering	54
2.4.6	Supercontinuum generation.....	56
3	EXPERIMENTAL	57
3.1	Z-scan and Optical Kerr-Gate	57
3.2	Femtosecond laser writing	58
3.3	Waveguide characterization coupling system	59
4	THIRD-ORDER OPTICAL NONLINEARITIES IN BULK AND FS-LASER INSCRIBED WAVEGUIDE IN STRENGTHENED ALKALI ALUMINOSILICATE GLASS [†]	63
4.1	Bulk nonlinearities of Gorilla [®] Glass.....	63
4.2	Femtosecond laser micromachining and waveguide inscription	65
4.3	Linear and nonlinear characterization of fs-inscribed waveguides	68
4.4	Partial conclusion.....	73
5	NONLINEAR OPTICAL WAVEGUIDES INSCRIBED BY FS-LASER IN ORGANIC CRYSTAL FOR BROADBAND SECOND HARMONIC GENERATION OF UV PULSES	75

5.1	Cladding waveguide structure	75
5.2	L-threonine crystal and experimental setup.....	76
5.3	Waveguide fs-laser inscription, linear and nonlinear characterization	78
5.4	Partial conclusion	84
6	CONCLUSIONS AND PESPECTIVES.....	85
	REFERENCES.....	87
	APENDIX A – List of publications and conference presentations.....	97

1 INTRODUCTION

The laser was first demonstrated in 1960 by Theodore H. Maiman¹ and it was rapidly inserted in science and technology as a fundamental tool for many applications. In addition, laser light gave rise to important new research lines, such as nonlinear optics. The first nonlinear optical effects observed were second harmonic generation² and two-photon absorption³, which were only possible due to the coherent intense light sources capable of producing fields with high enough intensities to perturb the motion of bound electrons in the medium in a nonlinear way. Simultaneously, laser started to be applied to material processing and the promising early results obtained boosted its way up to other main research fields, for example, engineering and medicine. Laser technological advances throughout the years provided lasers able to produce extremely intense ultrashort pulses, which pushed material processing through a revolution by opening new avenues for material ablation and inducing properties changes. By applying pulses with duration on the order of tens and hundreds of 10^{-15} seconds, material's modification with barely any heat affect zone outside the irradiated spot became possible, in the so called area of femtosecond (fs) laser micromachining.⁴ This brought a clear advantage over longer pulses, by increasing the precision and quality of the micro/nanostructures produced.⁵ Basic and fundamental research on the light-matter interaction at such extreme regime related fs-laser micromachining characteristics to nonlinear phenomena that take place during the process and its ultrafast dynamics.

Among metals, semiconductors and dielectrics, a wide range of materials have been micromachined via ultrashort pulse irradiation, with the majority of such experiments being performed using Ti:Sapphire laser sources, whose output spectrum is typically centered at around 800 nm, and with fiber laser at $\sim 1 \mu\text{m}$ that has gain popularity. Therefore, those materials can be divided in two classes regarding its linear absorption with respect to the pump excitation wavelength. Within the class of opaque materials, specifically for metals, the high spatially selective ablation obtained with fs-laser microstructuring have been used, for example, for repairing photolithography masks⁶, hole drilling⁷, production of reflecting computer generated holographic for security⁸⁻⁹ or beam control¹⁰⁻¹¹, maskless alternative fabrication of interdigitated electrodes for faster prototyping¹², nanoparticles generation¹³ and producing superhydrophobic surfaces.¹⁴ Still on non-transparent materials, such as linearly

absorbing semiconductors, their surface topography and properties have also been modified by ultrashort pulses. Fs-pulse irradiation of silicon resulted on the formation of Laser Induced Periodic Surface Structures (LIPSS)¹⁵⁻¹⁷ that drastically increased its absorption¹⁸⁻¹⁹, which has been proposed to improve solar cells and detectors performance. Structural morphology modifications represented by the amorphization and crystallization²⁰ have been reported as well.

For transparent materials, fs-microstructuring is entirely ruled by nonlinear absorption²¹, which due to its nonlinear dependence on the optical field intensity arises the possibility of inducing three-dimensional changes into the volume of the material, opening a number of possibilities for photonic applications. Glasses and polymeric compounds are some of the transparent materials used in ultrashort pulse micromachining, being the ones frequently used for development of optical devices. For example, optical data storage devices²², where bits are represented by micrometer-sized refractive index changed regions, are induced in the bulk of the material with a high numerical aperture microscope objective. Microfluidic channels fabrication²³ also uses the spatial selectivity to promote properties change inside glasses, such that upon chemical etching it gets etched in a much higher rate than the non-irradiated areas. The resulting hollow microchannels are frequently used on the development of lab-on-a-chip sensor.²⁴ Another distinct use of fs-laser pulses on transparent materials is the microfabrication of polymeric structures via two-photon absorption. In the presence of a photo-initiator, the initially liquid resin gets polymerized through a polymerization triggered via two-photon absorption, that only takes place at the high intense focal region of the beam.²⁵ This technique allows the fabrication of arbitrary three-dimensional structures on the micrometer scale with sub-wavelength resolution and its applications range from birefringent optical storage²⁶, photonics crystals²⁷, microlenses²⁸, microneedles²⁹, bacterial and cells microenvironment³⁰⁻³¹, micropixel³², microresonators³³, microlasers³⁴, to micropumps³⁵ composed by structures containing moving parts.

Amongst the many devices fabricated that make use of femtosecond pulses, laser inscribed waveguides have gained a great deal of attention because of its simple fabrication process and the promise of creating optical circuits for integrated photonics. By scanning the ultrafast laser beam focus inside the sample, a localized permanent modification of its refractive index is induced and a waveguide-like structure is created.³⁶ Extensive research has been carried out on fs-laser writing of waveguides

in several materials³⁶⁻³⁸, as well as different patterns to produce waveguide based devices, such as splitters³⁹, couplers⁴⁰⁻⁴¹, integrated waveplates⁴², Mach-Zehnder interferometers⁴³, Bragg fibers⁴⁴⁻⁴⁵ for sensors, ring resonators⁴¹ and etc. Although all these examples are considered the building blocks for more complex devices, they don't fill the complete list of requirements to achieve the goal of an all-optical photonic chip, with potential for faster and less power consuming signal processing technology, because they share the characteristic of being passive elements. The active elements needed for signal processing rely on nonlinear optical effects, which are favored by the high power being guided in small mode area through long interaction lengths in waveguide devices. Some of the nonlinear phenomena that occur in waveguides are second harmonic generation, self-phase modulation, cross-phase modulation, soliton formation, four-wave mixing, self-steepening, and stimulated Raman scattering. Therefore, it is extremely important studying not only the linear properties of the waveguide but also its nonlinear properties.

Another relevant matter for the development of optical devices is the proper choice of materials, which has shown to have a crucial role in their performance. For example, glassy materials are considered as promising candidates for robust platforms for photonics because of their interesting linear and nonlinear optical properties, which can be tailored by changing their chemical composition. Strengthened alkali aluminosilicate special glasses, such as Corning Gorilla[®] Glass, are present in more than four billion devices over the world mainly due to its outstanding mechanical and optical properties. Their commercial and technological impact, along with the advancements of ultrafast laser material processing has drawn interest to the use of Gorilla Glass as a platform for integrated optoelectronic devices. In late 2014, Gorilla Glass was reported to be an excellent matrix to host waveguide inscribed by femtosecond laser pulses.⁴⁶ Nevertheless, investigations about nonlinear optical properties from bulk Gorilla Glass and fs-laser inscribed waveguides have not been performed yet. This is one of the objectives of this dissertation.

As previously discussed, distinct materials and various technologies have been developed to accomplish miniaturized photonic integrated devices. Although the vast majority of the results reported in the literature are based on inorganic compounds²¹, organic materials have stood out for their ease of fabrication and functionalization which allows altering its optical, electrical and biological properties that can be designed for specific applications in soft photonics. In nonlinear optics, inorganic

crystals such as Potassium Dihydrogen Phosphate (KDP), Potassium Titanyl Phosphate (KTP) and β -Barium Borate (BBO), are used for frequency conversion based on their second-order nonlinearities and such features were successfully incorporated in waveguides produced via ultrashort pulses.⁴⁷⁻⁴⁹ Meanwhile, organic crystals, such as amino acid crystals, have shown interesting linear and nonlinear optical properties, which put them as promising candidates for nonlinear devices. By combining a wide transparency window, high second harmonic generation and low third order nonlinearities, the L-threonine amino acid crystal⁵⁰ was chosen in this dissertation project to host inscribed waveguide by fs-laser direct writing in order to produce a nonlinear waveguide capable of guiding and generating a second harmonic wave.

Overall, the main goal of this dissertation is to study the femtosecond laser inscription and characterization of nonlinear waveguides in Gorilla Glass and L-threonine organic crystals, exploring the specific bulk nonlinearities of each material. The further chapters of this dissertation are organized as follows: in Chapter 2, we present the fundamental concepts on nonlinear optics, ultrashort pulses, ultrafast material processing and nonlinearities in waveguides. In Chapter 3, we describe the experimental setups used to investigate materials nonlinear refractive index, to perform fs-laser micromachining and waveguide characterization. In Chapter 4, we present the study the nonlinear optical properties of Gorilla Glass bulk and written waveguides. In Chapter 5, the inscription, characterization and second harmonic generation of cladding waveguides in L-threonine organic crystals is reported. Finally, in Chapter 6, we present the conclusions and perspectives.

2 THEORETICAL BASIS

Chapter 2 addresses the theoretical basis on relevant topics for the understanding of results and discussions presented further in this dissertation. This chapter covers general concepts of nonlinear optics, ultrashort pulse generation, fundamentals of femtosecond laser material processing and nonlinear effects in waveguide structures leading to supercontinuum generation.

2.1 Nonlinear optics

The linear and nonlinear optical regimes can be differentiated by the intensity level of the electromagnetic wave travelling through the media. In linear optics, the amplitude of the electric field of the optical field is many orders of magnitude smaller than the interatomic electric field created by the atomic nucleus and its bound electrons. Therefore, such light-matter interaction can be treated by the Drude-Lorentz model⁵¹⁻⁵², that considers the electronic motion to follow a damped harmonic oscillator and, as result, shows the linear dependency of the induced polarization \vec{P} with respect to the electric field \vec{E} given by

$$\vec{P} = \varepsilon_0 \chi \vec{E} \quad (2.1)$$

in which ε_0 is the vacuum permittivity and χ is the electric susceptibility of the medium. By manipulating the Maxwell equations for isotropic transparent materials and using the constitutive relations, Eq. 2.1, the wave equation that determines the electromagnetic wave propagation in the media⁵¹

$$\nabla^2 \vec{E} - \frac{n^2}{c^2} \frac{\partial^2 \vec{E}}{\partial t^2} = 0 \quad (2.2)$$

is obtained. In this equation c is the light speed in vacuum and n is defined as the refractive index of the media that can be related to the material electronic susceptibility by

$$n = \sqrt{1 + \chi}. \quad (2.3)$$

In the case of nonlinear optics, the electric field amplitude produced of the optical wave becomes comparable to the interatomic electric field, making the Drude-Lorentz harmonic model approximation no longer valid and the electronic motion has to be treated as an anharmonic oscillator.⁵³ Such anharmonicity breaks the linear relationship between the induced polarization and the electric field, that is then usually described by an expansion in a power series of the electric field

$$\vec{P} = \varepsilon_0 \vec{\chi}^{(1)} : \vec{E} + \varepsilon_0 \vec{\chi}^{(2)} : \vec{E} \vec{E} + \varepsilon_0 \vec{\chi}^{(3)} : \vec{E} \vec{E} \vec{E} + \dots, \quad (2.4)$$

where $\vec{\chi}^{(j)}$ is the electronic susceptibility of j-th order. Meanwhile, the first order susceptibility $\vec{\chi}^{(1)}$ recovers the linear optics regime described by Eq. 2.1, higher order susceptibilities define the nonlinear optics, in which the induced polarization depends nonlinearly on the external electric field. Therefore, Eq. 2.4 can be rewritten as the sum of the linear and nonlinear polarizations, \vec{P}_L and \vec{P}_{NL} ,

$$\vec{P} = \vec{P}_L + \vec{P}_{NL} \quad (2.5)$$

stating that linear optics is a particular case of the more general nonlinear optics.

Similarly to the derivation of the linear wave equation (Eq. 2.2), but now using the polarization as in Eq. 2.4 and the relation for the speed of light in vacuum $c = 1/\sqrt{\varepsilon_0 \mu_0}$, we obtain the nonlinear wave equation that determines the electromagnetic wave in the nonlinear regime⁵³

$$\nabla^2 \vec{E} - \frac{n^2}{c^2} \frac{\partial^2 \vec{E}}{\partial t^2} = \frac{1}{\varepsilon_0 c^2} \frac{\partial^2 \vec{P}_{NL}}{\partial t^2} \quad (2.6)$$

As can be seen, the nonlinear polarization acts as source, generating new electric fields. It is important to mention that in nonlinear optics, it is often considered the interaction of two or more waves inside the media that can have the same or different frequencies. Therefore, the dispersive nature of materials expressed in the frequency dependence of electric susceptibility $\chi(\omega)$ and, consequently, its influence on the index of refraction $n(\omega)$ must be considered by solving Eq. 2.6 independently for each frequency involved in the nonlinear process.

To each nonlinear phenomenon there is a nonlinear susceptibility associated to it. For example, second-order nonlinear susceptibility that is behind nonlinear process as second harmonic, sum and difference frequency generation, and optical rectification. For second harmonic generation (SHG), let's consider a linear polarized input plane wave, E_1 , travelling in a non-centrosymmetric material, presenting a not null $\chi^{(2)}$, and its harmonic, E_2 , and second order nonlinear induced polarization. Here, for simplicity, the vector nature of the field has been omitted

$$E_1 = \frac{1}{2} (A_1(z) e^{i(k_1 z - \omega_1 t)} + c. c.) \quad (2.7)$$

$$E_2 = \frac{1}{2} (A_2(z) e^{i(k_2 z - \omega_2 t)} + c. c.) \quad (2.8)$$

$$P^{(2)} = \varepsilon_0 \chi^{(2)} E_1^2 = \frac{1}{4} [(\varepsilon_0 \chi^{(2)} A_1^2 e^{2i(k_1 z - \omega_1 t)} + c. c.) + 2\varepsilon_0 \chi^{(2)} E_1 E_1^*] \quad (2.9)$$

Thus, the nonlinear wave equation, Eq. 2.6, must be solved for the field oscillating at the harmonic frequency $\omega_2 = 2\omega_1$. Since the fields only depend on the longitudinal coordinate z , the operator ∇^2 can be replaced by d^2/dz^2 and we obtain

$$\frac{d^2 A_2}{dz^2} + 2ik_2 \frac{dA_2}{dz} = -\frac{\chi^{(2)} \omega_2^2}{c^2} A_1^2 e^{i(2k_1 - k_2)z}, \quad (2.10)$$

considering that the nonlinear effect isn't high enough to deplete the input fields amplitude (case of interest in this work). We may neglect the first term and by applying the Slowly Varying Amplitude Approximation (SVEA)⁵³, which is described by

$$\left| \frac{d^2 A_2}{dz^2} \right| \ll \left| k_2 \frac{dA_2}{dz} \right|. \quad (2.11)$$

By doing that, Eq. 2.10 gets reduced to

$$\frac{dA_2}{dz} = \frac{i}{2k_2} \frac{\chi^{(2)} \omega_2^2}{c^2} A_1^2 e^{i(\Delta k z)} \quad (2.12)$$

where the quantity Δk denominated as wavevector mismatch has been defined as

$$\Delta k = 2k_1 - k_2. \quad (2.13)$$

Finally, using that the intensity of the wave is given by the time-averaged Poynting vector

$$I_i = \frac{1}{2} n_i \varepsilon_0 c |A_i|^2, \quad (2.14)$$

and integrating Eq. 2.12 over the propagated distance L by the input waves inside the nonlinear material, we obtain the intensity of second harmonic generated as

$$I_2 = \frac{1}{2} \frac{|\chi^{(2)}|^2 \omega^2}{n_1^2 n_2 \varepsilon_0 c^3} L^2 I_1^2 \text{sinc}^2 \left(\frac{\Delta k L}{2} \right). \quad (2.15)$$

Besides the squared dependence on both, the fundamental wave input intensity and its propagated distance, it can be seen in Eq. 2.15 that the amount of second harmonic generated is strongly dependent on the phase mismatch parameter, shown in Fig. 2.1.

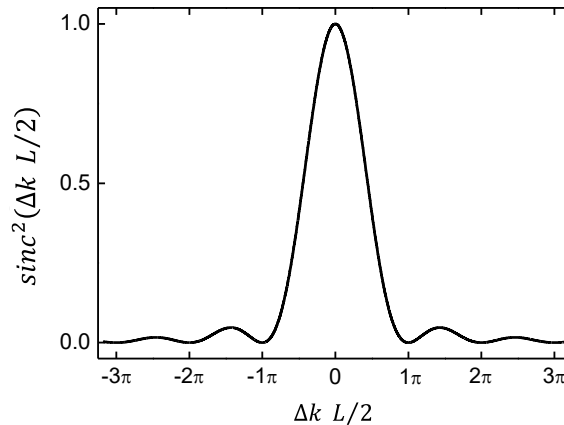


Figure 2.1 - Phase mismatch influence on the efficiency of second harmonic generation process.
Source: By the author.

As transparent materials in the normal dispersion regime (far from absorption) present a refractive index dispersion relation that can be described by an increasing monotonic function with respect to the wave frequency, efficient SHG cannot be achieved because the wavevector matching condition of $\Delta k = 0$ isn't satisfied. However, this issue can be resolved by making use of birefringent crystalline materials. The anisotropy intrinsic to crystals allows fields with different polarization orientations to experience distinct indexes of refraction, called ordinary and extraordinary. Such approach makes it possible that a given frequency and its second harmonic travel

within the material at the same speed, and so that the generated wave are added constructively throughout the nonlinear process.⁵³

Third order nonlinearities, such as third harmonic generation (THG) and the nonlinear refractive index, are associated with the nonlinear polarization that can be expressed in its explicitly form as

$$P^{(3)}(t) = \varepsilon_0 \chi^{(3)} E_1^3 \quad (2.16)$$

$$= \frac{1}{8} \varepsilon_0 \chi^{(3)} [(A_1^3 e^{3i(k_1 z - \omega_1 t)} + c. c.) + 3|A_1|^2 (A_1 e^{i(k_1 z - \omega_1 t)} + c. c.)].$$

The first term gives rise to a new wave oscillating at a frequency three times higher than the frequency of fundamental input wave. This is the phenomenon of THG, that similarly to SHG requires phase matching condition to be satisfied and is only efficient in crystals. Considering the second term in Eq. 2.16, that oscillates at the same frequency of the fundamental wave, the total induced polarization can be written as

$$P = P_L + P_{NL} = \varepsilon_0 \left(\chi^{(1)} + \frac{3}{4} \chi^{(3)} A_1^2 \right) E_1. \quad (2.17)$$

Using Eq. 2.14 it is possible to write the total electric susceptibility, containing its linear and nonlinear terms, as

$$\chi = \chi^{(1)} + \frac{3}{2} \frac{\chi^{(3)}}{c \varepsilon_0 n_0} I \quad (2.18)$$

where n_0 is the linear refractive index.

Recalling the relation between the refractive index and the electric susceptibility described in Eq. 2.3 and applying a Taylor expansion, since $\chi^{(3)}$ is much smaller than $\chi^{(1)}$, we obtain the nonlinear Kerr-optical effect that shows the intensity dependence of the index of refraction and define the nonlinear refractive index⁵⁴ n_2 as:

$$n \approx n_0 + n_2 I \quad (2.19)$$

$$n_2 = \frac{3}{4} \frac{\chi^{(3)}}{c \varepsilon_0 n_0^2}. \quad (2.20)$$

It is noteworthy that typical n_2 are rather small, being on the order of 10^{-20} m²/W for glassy materials.⁵⁵

2.2 Ultrashort pulse generation

An ultrashort laser pulse is one of the fastest phenomena ever created and consists of an electromagnetic optical pulse whose duration ranges from a femtosecond (10^{-15} s) up to a picosecond (10^{-12} s), has a broadband spectrum and extremely high peak power. Its generation requires a properly designed cavity composed by mirrors, lenses and dispersion compensation elements, a pump source, a gain medium with a wide emission spectrum and a mode locking mechanism.⁵⁶

The cavity geometry and the gain medium emission play a critical role in the laser output spectrum. The cavity acts a spectral filter because not all frequencies are allowed to oscillate inside it. Only resonant frequencies that have an accumulated phase of an integer multiple of 2π over a round trip in the cavity will interfere constructively to form oscillating stationary waves. Waves with dissonant frequencies that do not satisfy such condition are destroyed by destructive interference. Therefore, the resonant frequencies that compose the frequency comb of a laser cavity of length L is given by

$$\nu_m = m \frac{c}{2L}, \quad (2.21)$$

where m is a positive integer greater than zero. One can see from Eq. 2.21 that the number of modes allowed in a cavity is infinite. However, it doesn't determine which or how many modes are excited. This matter is addressed by the gain medium, which when excited by the pump source emits a continuum wide spectrum containing cavity resonant frequencies that start to oscillate. This discussion about the oscillating modes in a laser cavity is graphically represented in Fig. 2.2. In Fig. 2.2(a) it is shown the frequency comb of resonant frequencies allowed by the cavity. Figure 2.2(b) illustrates the emission gain spectrum of the laser medium, while Fig. 2.3(c) displays the combination of both, with the actual excited modes oscillating inside the cavity.

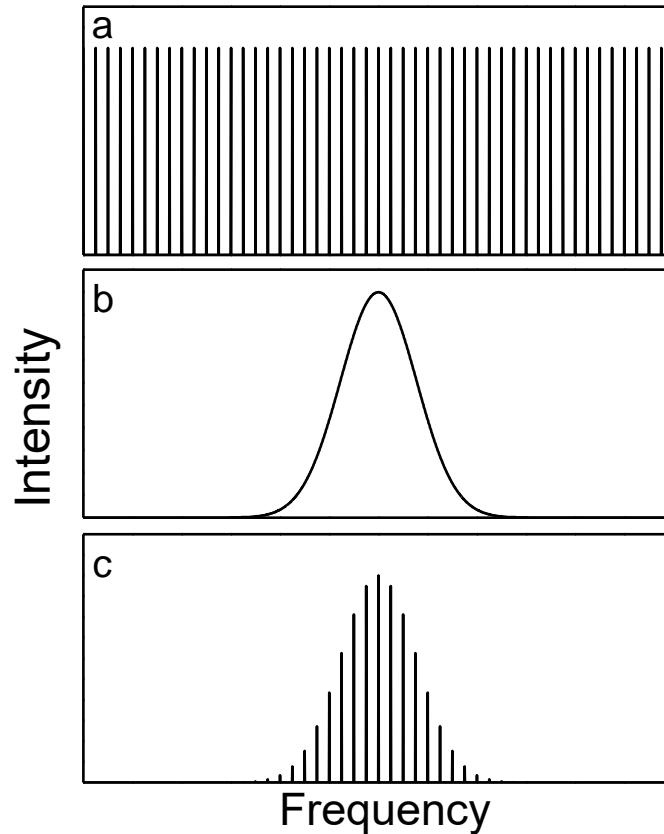


Figure 2.2 – Schematic representation of (a) cavity resonant frequency comb, (b) gain media emission spectrum and (c) the laser output spectrum.
Source: By the author.

The obligatory mode locking mechanism for ultrafast pulse generation requires a high number of modes oscillating in the cavity and so the appropriate choice of gain medium is crucial. Ti:Sapphire crystals have become very popular in ultrashort laser systems due to their excellent thermal and optical properties, such as high thermal conductivity, low thermal expansion, wide absorption spectrum around 500 nm and an extremely broadband emission centered at 790 nm, ranging approximately from 700 nm up to 1000 nm (~ 140 THz).⁵⁷ Considering a laser cavity length of 1 meter and using Eq. 2.21, we found that the resonant frequencies are separated by 150 MHz and, for a Ti:Sapphire gain medium, more than 9×10^5 modes can be oscillating in the cavity.

In a scenario of a highly excited cavity, the laser output is given by the sum of all propagating fields as

$$E(t) = \sum_{m=1}^N E_m \exp[-i(2\pi\nu_m t + \phi_m)] \quad (2.22)$$

where N is the number of modes excited frequency ν_m , amplitude E_m and phase ϕ_m . Since the field amplitudes may be altered by external factors and their phase can vary randomly, if any control mechanism is not applied the laser output turns out to be instable due to the interference of the many electric fields present in the cavity. Optical ultrashort pulses are formed when the phase of modes are locked with respect to each other.^{56,58} The concept of mode locking can be demonstrated by assuming the case in which the phase of each mode is null and its amplitudes are set as a constant, E_0 . The laser output intensity, which is proportional to the squared field amplitude, is shown in Fig. 2.3 for the case when the total number of modes inside the cavity is (a) 2, (b) 5, (c) 10, (d) 50 and (e) 100, and also for 100 modes but with random relative phases. From this, one can conclude that mode locking is primordial for pulse generation and that the laser pulse duration becomes shorter rapidly and its intensity gets considerably bigger as the number of modes increase. Because these pulses are ultrashort, they can achieve peak powers as high as MW (10^6 Watts) even though their average powers are on the order of mW (10^{-3} Watts).

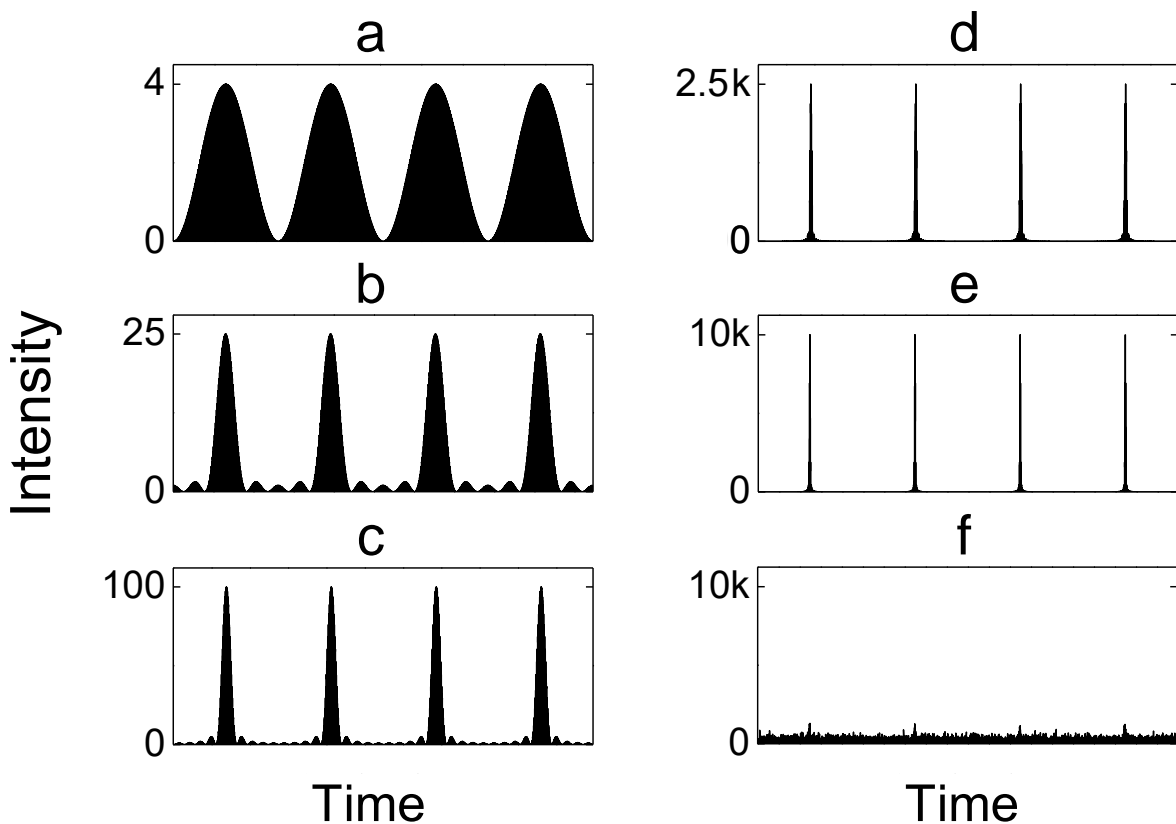


Figure 2.3 – Laser output intensity as a function of time in the mode locking regime with (a) 2, (b) 5, (c) 10, (d) 50 and (e) 100 modes, and the case for (f) 100 modes with random relative phases.

Source: By the author.

There are a number of ultrafast laser systems that have been developed. Oscillators are lasers that use a passive mode locking mechanism to generate pulses with duration on the order of 50 fs at a repetition rate of ~ 80 MHz (depending on the cavity length) and pulse energy up on the order of nJ. More complex designed laser systems are capable of amplification of such pulse energies by orders of magnitude and, for this reason, they are called amplified laser systems. Femtosecond pulse amplification must be performed with caution, since they can easily reach peak intensity high enough to cause damage to the optical elements in the cavity. To overcome this issue, a technique called chirped-pulse amplification (CPA) is applied.⁵⁹ The CPA process begins with a low energy fs-pulse that is temporally stretched by a pair of diffraction gratings, so its peak intensity is reduced enough to guarantee that the amplified stretched pulse doesn't damage the crystal or other optical elements. After its amplification, it is then compressed by another pair of gratings, resulting in a much more intense ultrashort laser pulse with energy on the order of μJ – mJ. Figure 2.4 illustrates the concepts involved in the chirped pulse amplification.

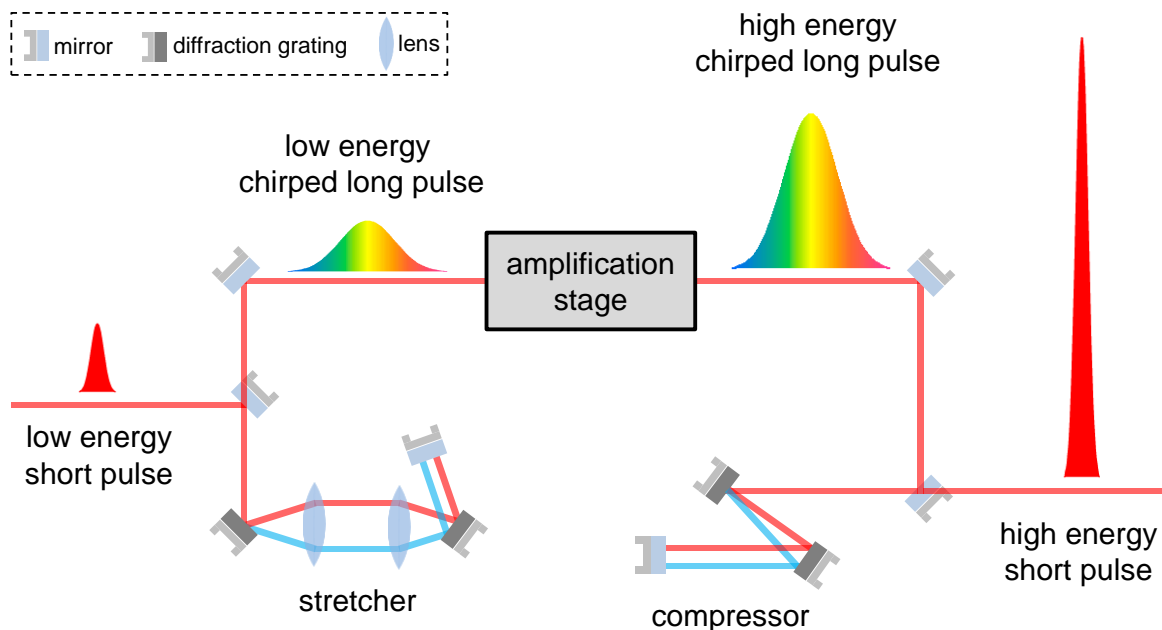


Figure 2.4 – Illustration of chirped-pulse amplification technique that makes use of an amplification stage, pulse stretcher and compressor.

Source: By the author.

The development and establishment of high intensity ultrashort pulse lasers greatly benefited research area as nonlinear optics and, specially, laser material processing.

2.3 Fundamentals of fs-laser material processing

Femtosecond laser micromachining is defined as the process in which ultrashort pulses are used to produce micrometer-sized features on the surface or inside the bulk of a solid material, and it was first demonstrated in 1995 by drilling holes with sub-micrometer diameter in a metal film.⁷ It relies on the optical breakdown that takes place when energy deposition from an optical field into a material leads to the ionization of a great amount of electrons, which then transfer such energy to the lattice causing permanent damage.

The outcome of microstructuring is strongly dependent on experimental parameters such as, for example, excitation wavelength, pulse duration and energy, laser repetition rate, focusing objective numerical aperture and scan speed. Moreover, it also depends on materials' optical and thermal properties, since they determine its response upon ultrashort light irradiation. Therefore, knowledge about how femtosecond pulses interact with matter is essential for understanding the process of ultrashort laser micromachining, which is governed by fundamentally different aspects when carried out with longer pulses.⁵

The remarkable high spatial selectivity in materials processed using ultrashort pulses is ensured by a couple of reasons. The first one is related to the fact that laser energy is deposited onto the target within the pulse duration, which is a time interval much shorter than the time required for any relaxation or thermalization processes to be initiated. In fact, such energy is absorbed just by the material electronic configuration, leading to a primary heating of the electrons while the atomic lattice remains nearly unaltered. Then, the highly excited electrons transfer the accumulated heat to the ions that start a thermalization process by diffusion, long after the pulse has left the material. Under these heavy non-equilibrium conditions, the electronic and lattice systems are decoupled and can be treated independently in the so-called Two-Temperature model.⁶⁰ The second reason is associated with light absorption mechanisms being governed by nonlinear processes due to the extremely high peak intensities delivered by ultrashort pulses. Both, linear and nonlinear absorption processes are illustrated in Fig. 2.5

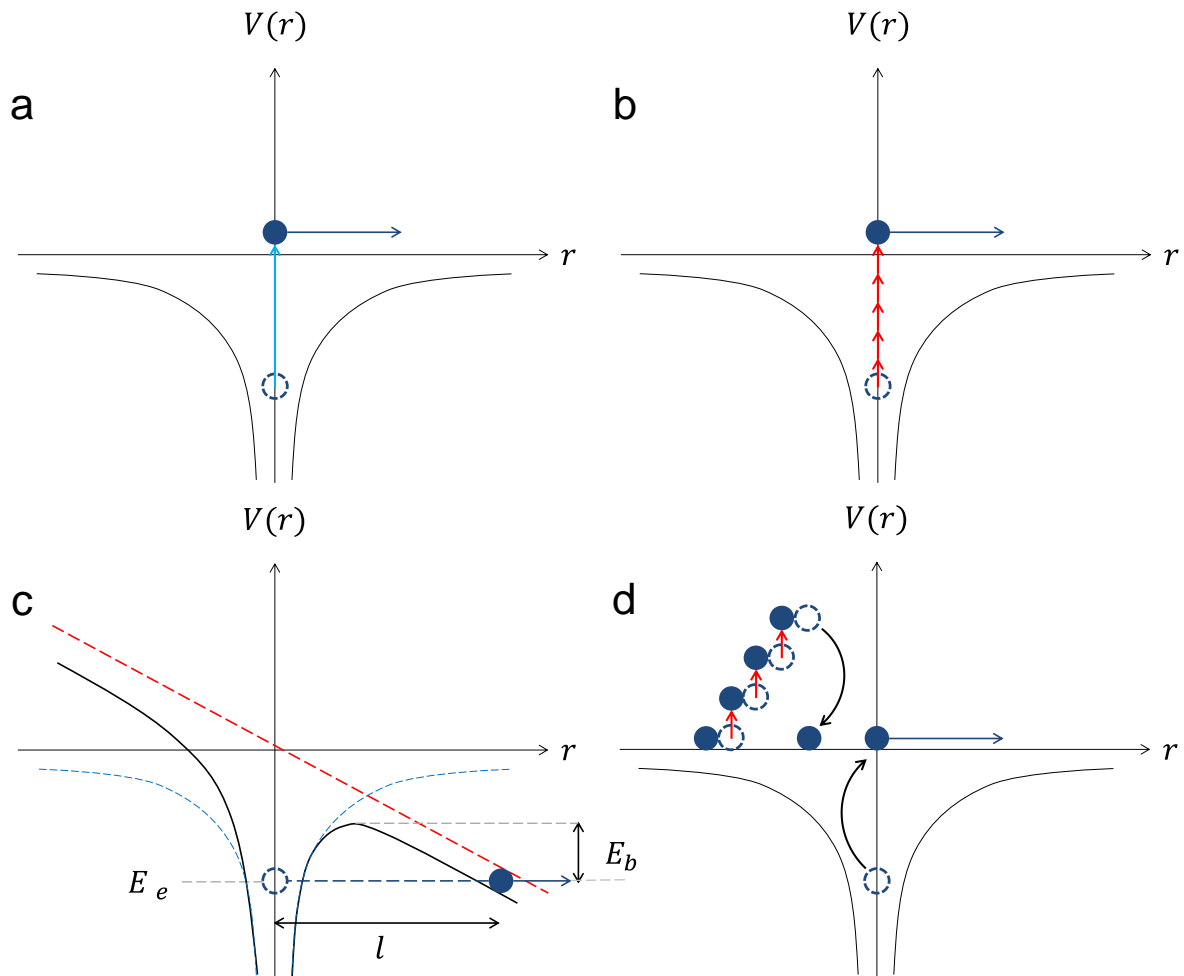


Figure 2.5 – Schematic illustration of (a) linear and nonlinear absorption classified by the process of (b) multiphoton, (c) tunneling and (d) avalanche ionization.

Source: By the author.

In linear absorption, shown in Fig. 2.5(a), an electron gets promoted from the valence band to the conduction band by absorbing a single photon, which must have energy, $\hbar\omega$, equal or greater than the gap energy, E_g , between those bands. In contrast, nonlinear absorption involves a collection of photons with less energy than the required to produce linear absorption ($\hbar\omega < E_g$), acting together to leave the material excited or ionized. The nonlinear absorption mechanisms may be divided in three different types. In multiphoton ionization, represented in Fig. 2.5(b), a single electron in the valence band absorbs n photons to be promoted to the conduction band. In order to achieve multiphoton ionization, the sum of all energy photons participating has to be greater than the energy gap ($n\hbar\omega > E_g$). Nonlinear photoionization may also occur via tunneling process assisted by the distortion of the atomic potential induced by the high intensity laser electric field, as in Fig. 2.5(c). Both nonlinear processes, multiphoton and tunneling ionization, were studied by Keldysh⁶¹ in 1965 and showed

to be distinct regimes of the same phenomenon, differentiated by the laser intensity and wavelength.

The Keldysh parameter (γ_K) distinguishes which mechanism dominates the nonlinear photoionization, by determining whether the light-matter interaction that frees an electron from the atomic binding potential can be described as a picture of an electrostatic tunneling.⁶² In order to do so, a semiclassical approach is used to estimate the time the electron takes to cross the barrier and compare it with the period of the incident light. In the case that the electron tunneling time is shorter than the light oscillating period, the optical field can be treated as a static field tilting the binding potential. The tunneling time is estimated by dividing the width of the barrier by the electron velocity in the barrier.

Let the total potential energy be

$$V(r) = U(r) + xe\tilde{E}_0 \quad (2.23)$$

being $U(r)$ the Coulomb potential and \tilde{E}_0 the electric field peak amplitude. As it can be seen in Fig. 2.5(c), the potential is dropped by the binding energy E_b along the length l and the width of the potential barrier is

$$l = \frac{E_b}{e\tilde{E}_0}. \quad (2.24)$$

Energy conservation shows that the electron velocity within the barrier has a pure imaginary value, since $V(r)$ is greater than the bound electron energy E_e and its modulus is given by

$$|v(r)| = \sqrt{\frac{2(V(r) - E_e)}{m_e}} \quad (2.25)$$

where m_e is the electron effective mass. Considering the escape of the slowest electron, it enters the barrier satisfying $E_b = V(r) - E_e$, which leads to

$$|v(r)| = \sqrt{\frac{2E_b}{m_e}}. \quad (2.26)$$

Throughout the propagation in the barrier, the electron is slowed down reaching zero velocity at its end, since $V(r) = E_e$. In this way, the average electron velocity in the barrier can be roughly evaluated as the mean between the entrance and exit velocity

$$\langle |v| \rangle = \sqrt{\frac{E_b}{2m_e}} \quad (2.27)$$

and, consequently, tunneling time is given by

$$t_{tun} = \frac{l}{\langle |v| \rangle} = \frac{\sqrt{2m_e E_b}}{e\tilde{E}_0}. \quad (2.28)$$

It is convenient now to define the peak tunneling “frequency” as $\Omega_{tun} = 1/t_{tun}$ in order to present the Keldysh parameter

$$\gamma_K = \frac{\omega_0}{\Omega_{tun}} = \frac{\omega_0}{e} \sqrt{\frac{m_e \epsilon_0 c n E_b}{I}} \quad (2.29)$$

where the peak field amplitude \tilde{E}_0 was replaced by the laser peak intensity I following the relation from Eq. 2.14.

The multiphoton absorption picture displayed in Fig. 2.5(b) is associated with $\gamma_K \gg 1$, in which the laser frequency oscillates too quickly such that the electron doesn't feel the distortion of the binding potential, not allowing the electron tunneling. The tunneling picture in Fig. 2.5(c) is associated with $\gamma_K \ll 1$, where the optical field varies slowly enough to satisfy the “static-field approximation”. For practical means it is important to know how much smaller than unity should γ_K be for the nonlinear ionization process still be dominated by electron tunneling. Such question was addressed experimentally by Ilkov et al.⁶³ and determined that for Keldysh parameters $\gamma_K < 0.5$ ionization lies in the tunneling rather than in the multiphoton regime.

The last nonlinear absorption mechanism illustrated in Fig. 2.5(d) is the avalanche ionization, that combines free-carrier absorption and impact ionization.⁶⁴⁻⁶⁵ Initially, an electron already in the conduction band absorbs subsequent photons increasing its energy to a level that exceeds the minimum of the conduction band by

at least the gap energy. Then, this extremely excited electron promotes an electron from the top of the valance band by impact ionization, which is an energy exchange mechanism via collision resulting in both electrons at the bottom of the conduction band. The process starts over again with both electrons as primary electrons to promote other two electrons to the conduction. The name avalanche ionization is due to the fact that the mechanism repeats itself during the pulse duration making the electronic population in the excited state increases exponentially. For the process to get started, an initial electron usually called as seed is required and, in the case of fs-laser pulses, it may be created via multiphoton ionization or come from defect states closer to the conduction band. The extremely high density of electron in the excited state leads to a plasma formation that becomes opaque to the incident laser frequency and energy absorption from the optical field is strongly enhanced.

In general, ultrashort laser material processing is classified in ablation and damage. Ablation takes place at surfaces and its main characteristic is the material removal that occurs in a timescale on the order of hundreds of nanoseconds.⁶⁶ The non-equilibrium conditions bring complexity to the physical mechanisms involved, such as Coulomb explosion, material ejection and evaporation. The minimal heat affected zone produced in the surroundings of laser spot region gives femtosecond laser ablation great spatial selectivity, which is attributed to the significant amount of energy spent in material removal at the initial stages and less heat diffuses into the lattice.

Bulk damage is exclusive to transparent materials since nonlinear absorption is highly dependent on laser intensity and only takes place in focal volume, where intensity is high enough to produce ionization leading to material modification. This feature allowed the microfabrication of three-dimensional structures into materials bulk while keeping regions outside the beam focus intact. The main structural modifications observed in bulk damage can be divided in two categories regarding the laser energy level with respect to material threshold. If pulse energy is below the threshold for material ablation, changes in the refractive index are produced due to material melting and subsequent fast resolidification.⁶⁷⁻⁶⁸ Such changes in the index of refraction may be positive or negative, depending if the material density has increased or decreased upon the rapid cooling.⁶⁹⁻⁷¹ In the opposite case, in which pulse energy is above material ablation threshold, the formation of empty voids are observed resulting from microexplosions causing material to expand, producing a hollow or relatively less dense region in the focal volume.^{22,72-74}

As discussed, knowledge of the energy threshold for material ablation is crucial for defining the proper experimental parameters for device fabrication. A method to determine the ablation threshold was proposed by Liu,⁷⁵ according to the following. Consider a temporal and spatial Gaussian pulse, whose intensity can be written as

$$I(r, t) = I_0 e^{-\left(\frac{t}{\tau}\right)^2} e^{-\left(\frac{r}{\rho}\right)^2} \quad (2.30)$$

where I_0 is the peak intensity, and τ and ρ are the characteristics temporal and spatial radii, respectively. The pulse spatial distribution of energy fluence is obtained by integrating the intensity in time resulting in

$$F(r) = F_0 e^{-\left(\frac{r}{\rho}\right)^2}, \quad F_0 = \sqrt{\pi}\tau I_0 \quad (2.31)$$

with peak fluence F_0 .

If this pulse is focused on a target material surface, it will produce a circular ablation region with radius r_{th} that has an associated threshold fluence F_{th} . This scenario is illustrated in Fig. 2.6 by the black curve.

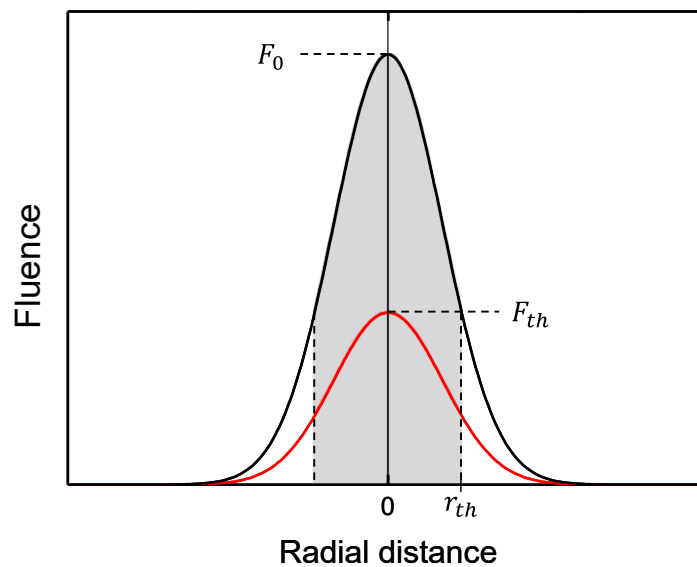


Figure 2.6 – Pulse fluence as a function of the radial distance with two different peak fluences.
Source: By the author.

Thus, the ablation threshold fluence of this material can be determined by performing ablation experiments with different pulse peak fluences, measuring their threshold radii and using

$$r_{th}^2 = \rho^2 \ln \frac{F_0}{F_{th}}. \quad (2.32)$$

However, it would be more practical to work with pulse energy rather than fluence, since accurate fluence measurements are difficult due to the small spot sizes of focused beams. The energy E_p of a pulse is obtained by integrating its fluence in space and is related to the its peak fluence by

$$E_p = F_0 \pi \rho^2. \quad (2.33)$$

The red curve in Fig. 2.6 shows that it is possible to set a pulse with peak fluence to match the threshold fluence and, therefore, find the threshold energy of a pulse to produce ablation using Eq. 2.33. Therefore, knowing that pulse spatial radii relates with beam waist by $\rho^2 = w_0^2/2$, Eq. 2.32 can be expressed in terms of pulse energy and pulse energy threshold

$$r_{th}^2 = \frac{w_0^2}{2} \ln \frac{E}{E_{th}}. \quad (2.34)$$

Besides pulse intensity, temporal width and wavelength, there are other experimental parameters that deeply influence the outcome of ultrashort pulses material processing, such as laser repetition rate. As previously mentioned, energy from the optical field is deposited in the material electronic system that gets highly excited and only after the pulse is gone it thermalizes with the lattice, so that, heat takes on the order of 1 μ s to leave the focal volume. Hence, the time in between adjacent pulses affects fs-laser micromachining, that can be carried out in two distinct regimes.⁷⁶ A cumulative behavior is observed when using oscillator lasers that emit pulses at a repetition rate of tens of MHz, since subsequent pulses hit the sample in a much shorter time than the characteristic time for heat to diffuse out of the focal volume. A repetitive regime is observed when using amplified lasers, that operate at a kHz repetition rate, and pulses are separated by a much larger time than the characteristic time for heat diffusion. As a result, before the next pulse arrives, equilibrium has been restored providing less energy accumulation and, consequently, barely any collateral damage in the laser spot vicinities.

2.4 Nonlinear effects in waveguide structure

A typical waveguide structure is based on the total internal reflection phenomenon that occurs when a travelling wave hits an interface with a different material of a lower refractive index, at an incident angle higher than the critical angle, defined by the Snell's law. There are several waveguides structures, with different geometrical and optical features. Here, however, we will use step-index profile to develop the theoretical basis of cylindrical waveguides, pulse propagation and some nonlinear effects.

2.4.1 Waveguide structure and pulse propagation

A step-index optical fiber consists of a cylindrical inner core of refractive index n_1 and radius a , wrapped by an outer cladding of slightly lower refractive index n_2 , as illustrated in Fig. 2.7. Its name is a reference to the index profile that abruptly changes at the point where the core material meets the cladding material.⁷⁷

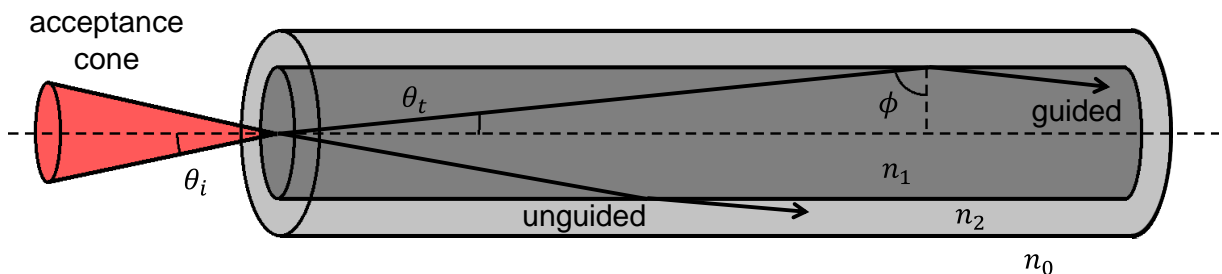


Figure 2.7 – Step-index optics fiber illustration, acceptance cone, guided and unguided rays.
Source: Adapted from SALEH.⁷⁷

An input ray experiences a refraction at the entrance of the waveguide that is described by the Snell's law

$$n_0 \sin \theta_i = n_1 \sin \theta_t \quad (2.35)$$

and will be guided by total internal reflections at the core-cladding interface if its incident angle ϕ is greater than the critical angle given by

$$\sin \phi_c = \frac{n_2}{n_1}. \quad (2.36)$$

The biggest input angle θ_i that still satisfy the critical angle condition to be guided determines the acceptance cone of the waveguide and defines the waveguide Numerical Aperture (NA)⁷⁷, that represents the light-coupling capacity of the waveguide, and is given by

$$NA = n_0 \sin \theta_i^{max} = \sqrt{n_1^2 - n_2^2}. \quad (2.37)$$

One can see that a greater refractive index difference between the core and the cladding leads to higher NA and, consequently, a bigger acceptance angle.

With some of the geometrical and ray optical features of the step-index waveguide presented, let's investigate, from the wave perspective, the electromagnetic field propagation within such structure by solving the wave equation. From the wave equation in Eq. 2.2 and assuming that the electric field of the propagating wave is represented by

$$E(z, t) = A(\vec{r})e^{i(kz - \omega t)}, \quad (2.38)$$

we obtain the Helmholtz equation

$$\nabla^2 E + n^2(\omega)k_0^2 E = 0 \quad (2.39)$$

since $k_0 = \omega/c$. Taking advantage of the cylindrical symmetry of the studied waveguide, the Helmholtz equation can be rewritten in the cylindrical coordinates depending on (r, ϕ, z) as

$$\frac{\partial^2 A}{\partial r^2} + \frac{1}{r} \frac{\partial A}{\partial r} + \frac{1}{r^2} \frac{\partial^2 A}{\partial \phi^2} + \frac{\partial^2 A}{\partial z^2} + n^2 k_0^2 A = 0 \quad (2.40)$$

where the amplitude of the field is a function of cylindrical coordinates $A(\vec{r}) = A(r, \phi, z)$, and the refractive index n admits the value of n_1 if $r \leq a$ and n_2 if $r > a$. Since the guided waves are propagating in the z direction with propagation constant β and are periodic with ϕ over a 2π rotation, the amplitude is

$$A(r, \phi, z) = F(r)e^{-i\beta z}e^{-im\phi}, \quad m = 0, \pm 1, \pm 2, \pm 3, \dots \quad (2.41)$$

By using the variable separation method, we get the equation for the radial profile of the field as

$$\frac{\partial^2 F}{\partial r^2} + \frac{1}{r} \frac{\partial F}{\partial r} + \left(n^2 k_0^2 - \beta^2 - \frac{m^2}{r^2} \right) F = 0 \quad (2.42)$$

Equation 2.42 is denominated the Bessel equation and its solutions are expressed by the Bessel functions of the first and second kind ($J_m(r)$ and $Y_m(r)$), and its modified versions ($K_m(r)$ and $I_m(r)$). However, by using physical arguments that field amplitude cannot approach ∞ at $r = 0$ inside the core or when $r \rightarrow \infty$ in the cladding, we obtain that

$$F(r) \propto \begin{cases} J_m(k_t r), & r \leq a \\ K_m(\gamma r), & r > a \end{cases} \quad (2.43)$$

in which the parameters are defined as

$$k_t = \sqrt{n_1^2 k_0^2 - \beta^2} \quad (2.44)$$

$$\gamma = \sqrt{\beta^2 - n_2^2 k_0^2}. \quad (2.45)$$

The fields in the core and the cladding, and consequently its parameters k_t and γ , are tied by the boundary conditions at its interface, which implies that both amplitude and its derivate must be continuous. From such constrains and using the Bessel functions derivative identities relations, we obtain the transcendental equation for β and the definition of the normalized frequency V-number

$$(k_t a) \frac{J_{m\pm 1}(k_t a)}{J_m(k_t a)} = \mp(\gamma a) \frac{K_{m\pm 1}(\gamma a)}{K_m(\gamma a)} \quad (2.46)$$

$$V = a \sqrt{k_t^2 + \gamma^2} = k_0 a NA \quad (2.47)$$

that determines which and how many modes are allowed in the waveguide structure.

For many applications it is desired that the guided mode is the fundamental one. Such single-mode waveguides have to be properly designed in such a way that Eq. 2.46 has only one root and this condition is satisfied when the normalized frequency of the waveguide is lower than 2.405.⁷⁷ The linearly polarized electric field of a mono-mode waveguide is given by

$$E(r) = \begin{cases} E_0 J_0(k_t r) e^{i\beta z}, & r \leq a \\ E_0 \frac{J_0(k_t a)}{K_0(\gamma a)} K_0(\gamma r) e^{i\beta z}, & r > a \end{cases} \quad (2.48)$$

The main linear optical effect that pulses propagating in waveguides undergo is attenuation or losses. Such losses are usually represented in dB per length unity and defined as

$$\alpha_{dB} = \frac{-10}{L} \log\left(\frac{P_f}{P_i}\right) \quad (2.49)$$

where P_i is the initial optical power being guided and P_f is the final optical power after a propagated distance L .

Other important effect is chromatic dispersion, that is responsible for the spread of optical pulses in time as they travel through the waveguide. This effect has different origins; it may be due to the material dispersion or waveguide related dispersion, such as guiding and modal, but the final outcome is a combination of contribution from all sources. Assuming a pulse composed by a superposition of waves in a single-mode waveguide, after a propagated distance z each frequency component ω will have accumulated a phase $\beta(\omega)z$, where $\beta(\omega)$ is the propagating constant and it is related with the refractive index of the guided mode by

$$\beta(\omega) = \frac{\omega}{c} n(\omega). \quad (2.50)$$

By expanding $\beta(\omega)$ in a Taylor's series around the pulse central frequency ω_0

$$\beta(\omega) = \beta_0 + \left. \frac{d\beta}{d\omega} \right|_{\omega_0} (\omega - \omega_0) + \frac{1}{2} \left. \frac{d^2\beta}{d\omega^2} \right|_{\omega_0} (\omega - \omega_0)^2 + \frac{1}{3!} \left. \frac{d^3\beta}{d\omega^3} \right|_{\omega_0} (\omega - \omega_0)^3 + \dots \quad (2.51)$$

with $\beta_0 = \beta(\omega_0)$. From the first derivate we have

$$\beta_1 \equiv \frac{d\beta}{d\omega} = \frac{1}{c} \left(n(\omega) + \omega \frac{dn}{d\omega} \right) = \frac{n_g}{c} = \frac{1}{v_g} \quad (2.52)$$

where we have defined the group refractive index $n_g = n(\omega) + \omega dn/d\omega$ and the group velocity $v_g = 1/\beta_1$. From the second derivate we found the group velocity dispersion (GDV) that is given by

$$\beta_2 \equiv \frac{d^2\beta}{d\omega^2} = \frac{-1}{v_g^2} \frac{dv_g}{d\omega}, \quad (2.53)$$

and provides information on how the group velocity varies with the frequencies within the pulse. This property is represented by the dispersion coefficient D of the waveguide, which is defined as the time delay per wavelength over a unity length, being given by

$$D = -\frac{2\pi c}{\lambda^2} \beta_2 \quad (2.54)$$

that gives information on how the group velocity varies with the frequency; therefore it is called waveguide dispersion parameter.

Figure 2.8 displays a typical dispersion coefficient for a silica-glass optical fiber as function of the wavelength.⁷⁸ As it can be seen, waveguide dispersion can be classified in three regimes. The normal dispersion regime is referred to negative dispersion coefficients ($D < 0$) and correspond to the scenario in which longer wavelengths propagate faster than shorter ones. The anomalous dispersion regime is the opposite; it is assigned to positive dispersion coefficients ($D > 0$) and represent the condition in which shorter wavelengths are faster. The last condition is when the dispersion coefficient is zero ($D = 0$), meaning that at the zero-dispersion wavelength ($\lambda_0 = 1.31 \mu m$ for silica) the wavelengths travels with same speed.

If the light being guided within the waveguide reaches high enough intensities, the induced polarization responds nonlinearly with the applied electric field, giving rise to nonlinear phenomena. In waveguides, such nonlinear effects can be very significant because guided waves have relatively small mode areas,

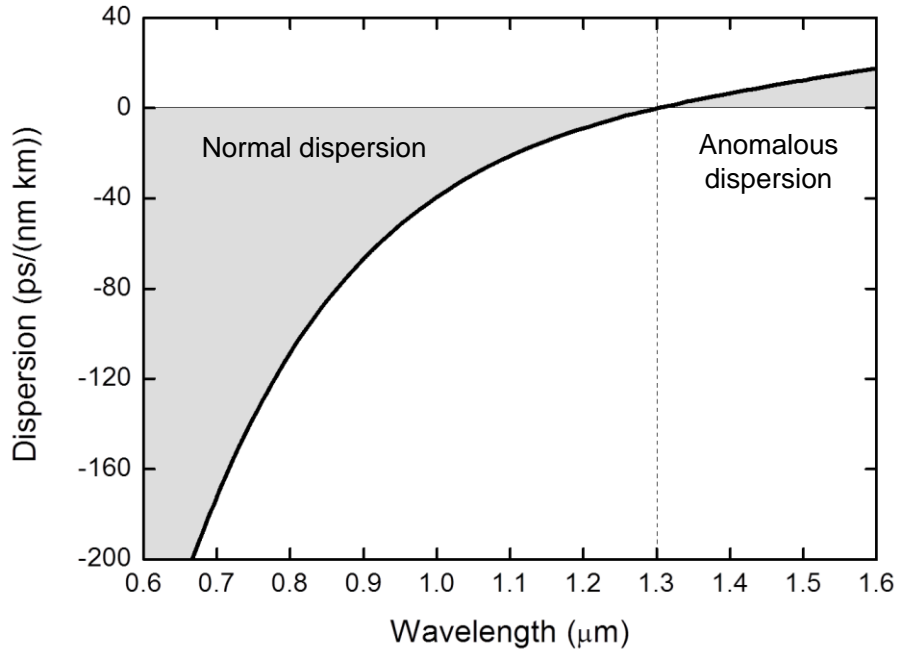


Figure 2.8 – Dispersion coefficient D of silica optical fiber as function of the wavelength.
Source: Adapted from AGRAWAL.⁷⁸

which favors higher intensity levels. Furthermore, the long interaction effective length, defined as the distance in which the optical intensity is kept high enough, also contributes to induce high nonlinear effects (by accumulation). Therefore, to study the nonlinear effects that take place during the propagation of intense optical pulses in waveguide, we must solve the nonlinear wave equation

$$\nabla^2 E - \frac{n^2}{c^2} \frac{\partial^2 E}{\partial t^2} = \mu_0 \frac{\partial^2 P_{NL}}{\partial t^2}. \quad (2.55)$$

From the electromagnetic analysis of waves travelling in cylindrical step-index single mode waveguides, we can write that the propagating field has a transversal, $F(r)$, and a longitudinal, $A(z)$, parts in the form of

$$E = F(r)A(z)e^{i(\beta_0 z - \omega_0 t)}. \quad (2.56)$$

By substituting the field expression (Eq. 2.56) in the nonlinear wave equation (Eq. 2.55) and taking into account all appropriate simplifications during the manipulation, it gets reduced to the nonlinear Schrödinger equation (NLSE)⁷⁸

$$i \frac{\partial U}{\partial z} - \frac{1}{2} \beta_2 \frac{\partial^2 U}{\partial \tau^2} + \gamma |U|^2 U = 0 \quad (2.57)$$

where the normalized amplitude U is

$$U = BA(z), \quad B = \pi \varepsilon_0 c n \int |F(r)|^2 r dr \quad (2.58)$$

with the nonlinear coefficient γ is defined as

$$\gamma = \frac{\omega n_2}{c A_{eff}} \quad (2.59)$$

in which A_{eff} is the modal effective area calculated by

$$A_{eff} = \frac{2\pi \left(\int_0^\infty |F(r)|^2 r dr \right)^2}{\int_0^\infty |F(r)|^4 r dr} \quad (2.60)$$

and is represented in a moving frame with the group velocity by the dislocated time

$$\tau = t - \frac{z}{v_g} \quad (2.61)$$

Here we are focusing on the interpretation of effects predicted by the nonlinear Schrödinger equation and its complete derivation can be found in reference ⁷⁹. An insightful representation of the NLSE is its normalized form because it introduces a couple of characteristic parameters. Defining a normalized amplitude Q according to

$$U(z, \tau) = \sqrt{P_0} Q(z, \tau) \quad (2.62)$$

where P_0 is the peak power of the incident pulse, and a normalized time coordinate

$$T = \frac{\tau}{t_0} = \frac{t - z/v_g}{t_0} \quad (2.63)$$

where t_0 is the temporal width of the pulse at the waveguide input. Eq. 2.57 becomes

$$i \frac{\partial Q}{\partial z} \pm \frac{\text{sgn}(\beta_2)}{2} \frac{1}{L_D} \frac{\partial^2 Q}{\partial T^2} + \frac{1}{L_{NL}} |Q|^2 Q = 0 \quad (2.64)$$

with the waveguide dispersion length

$$L_D = \frac{t_0^2}{|\beta_2|} \quad (2.65)$$

being the distance which a Gaussian temporal pulse needs to propagate to have its duration increased by $\sqrt{2}$. In Eq. (2.64) the waveguide nonlinear length is given by

$$L_{NL} = \frac{1}{\gamma P_0} \quad (2.66)$$

and represents the distance required for the pulse to accumulate a nonlinear phase of 1 rad.

Before discussing the nonlinear effects described by the NLSE in waveguides, it is worth mentioning that this equation is consistent with the linear cases if the nonlinear coefficient is neglected, resulting in a propagating pulse that gets chirped and stretched in time.

2.4.2 Self-phase modulation and optical soliton

The self-phase modulation (SPM) experienced by a pulse propagating in a waveguide is a manifestation of the material's refractive index dependence with the light intensity.⁷⁸ To isolate this phenomenon in the NLSE (2.57), we neglect the waveguide dispersion ($\beta_2 = 0$) and it is reduced to

$$\frac{\partial U}{\partial z} = i\gamma|U|^2U \quad (2.67)$$

with an amplitude general solution given by

$$U(z, \tau) = U(0, \tau)e^{i\phi_{NL}(z, \tau)} \quad (2.68)$$

and a nonlinear-induced phase change

$$\phi_{NL}(z, \tau) = \gamma|U|^2z . \quad (2.69)$$

This result indicates that the waveguide nonlinearity produces a modulation in the pulse phase proportional to its own intensity ($U^2 \propto I$) and the propagated distance. Using Eqs. (2.56) and (2.58), we can retrieve the electric field for the Gaussian temporal pulse centered at frequency ω_0 as

$$E(z, t) = E_0(\tau) e^{i[(\beta_0 + \gamma |E_0(\tau)|^2)z - \omega_0 t]} \quad (2.70)$$

where

$$E_0(\tau) = \mathcal{A}_0 e^{-\frac{1}{2} \left(\frac{\tau}{t_0}\right)^2}, \quad \tau = t - \frac{z}{v_g} \quad (2.71)$$

and the instantaneous frequency is given by definition as

$$\omega(t) = -\frac{\partial \phi}{\partial t} = \omega_0 + \gamma \frac{2\tau}{t_0^2} |\mathcal{A}_0|^2 e^{-\left(\frac{\tau}{t_0}\right)^2} z \quad (2.72)$$

Recognizing that the pulse squared field amplitude is proportional to its intensity ($|E_0(\tau)|^2 \propto I(\tau)$), in Fig. 2.9 it is plotted the pulse intensity and the induced frequency shift ($\Delta\omega = \omega - \omega_0$) are plotted as a function of the dislocated time of the moving frame travelling with the pulse

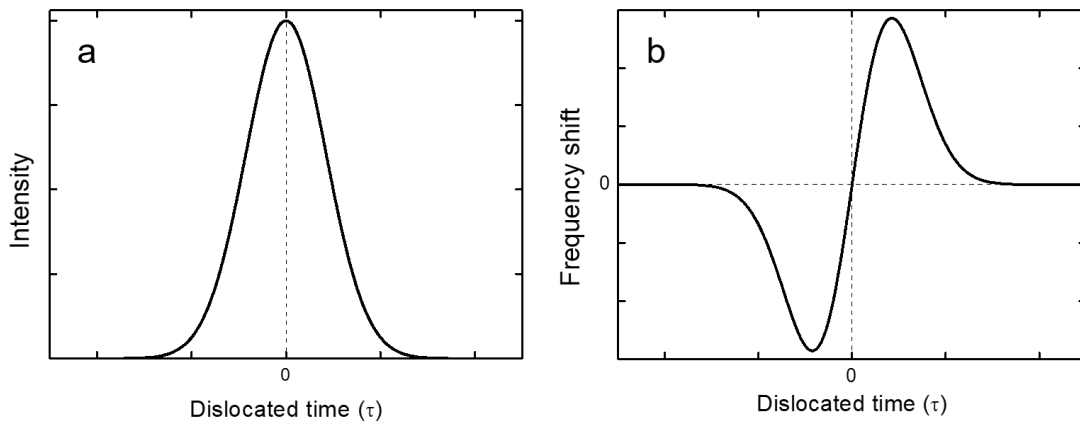


Figure 2.9 – Pulse (a) intensity and the (b) induced frequency shift as function of the dislocated time. Source: By the author.

As it can be seen, the induced frequency shift in the front of the pulse ($\tau < 0$) is negative, indicating the generation of lower frequencies with respect to the central frequency, whereas in the back of the pulse ($\tau > 0$) the induced frequency shift is

positive, indicating the generation of higher frequencies. Therefore, it shows that at the nonlinear regime the propagating pulse will get symmetrically chirped due to SPM, even neglecting the waveguide dispersion, as one can see in Fig. 2.10. Spectral broadening produced by self-phase modulation effect is crucial for generating an ultra-wide spectral pulse, known as supercontinuum.⁸⁰

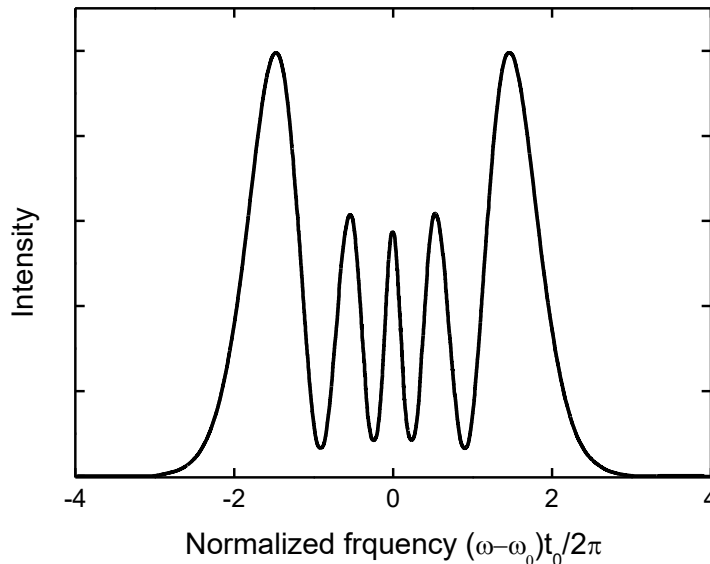


Figure 2.10 – Spectral broadened pulse via self-phase modulation effect.
Source: Adapted from AGRAWAL.⁷⁸

Waveguides, that guide many frequencies at the same time, may experience a similar nonlinear effect of intensity dependent phase induction, named cross-phase modulation (XPM).⁷⁸ This nonlinear phenomenon takes place when a frequency has its phase modulated nonlinearly by a different high intensity frequency being guided simultaneously and is relevant for applications, such as multiplexing and demultiplexing waveguides.

In the case that the waveguide dispersion cannot be neglected, it plays a major role in combination with the self-phase modulation effect and its influence can be divided by the dispersion regime. When the waveguide is operating on the anomalous regime ($D > 0$), the downshifted frequencies generated in the frontal part of the pulse and the upshifted frequencies generated in the trailing part by SPM move towards the center of the pulse, compressing it during propagation. In other words, the effect produced by dispersion is undone by SPM, and vice-versa. There is a possibility that both effects balance and cancel each other; as a result the pulse propagates without getting its shape distorted. The pulse in this particular condition is called a soliton.⁸⁰ Optical solitons are extremely important for nonlinear effects in waveguides and fiber

optics telecommunication systems. For waveguides under normal dispersion regime ($D < 0$), the downshifted frequencies generated in the frontal part of the pulse and the upshifted frequencies generated in the trailing part by SPM move away from the center of the pulse, stretching it as it travels.

2.4.3 Four-wave mixing

Four-wave mixing (FWM) is a nonlinear parametric process associated with the third order susceptibility $\chi^{(3)}$, that describes the interaction between four waves oscillating at frequencies ω_1 , ω_2 , ω_3 and ω_4 , being classified in two types. In the first one, three photons transfer their energy to a single new photon satisfying

$$\omega_4 = \omega_1 + \omega_2 + \omega_3. \quad (2.73)$$

If this case is degenerated ($\omega_1 = \omega_2 = \omega_3$), third harmonic generation is retrieved. In the second case of FWM, a pair of photons at frequencies ω_1 and ω_2 are annihilated to create a new pair of photons at frequencies ω_3 and ω_4 such that

$$\omega_4 + \omega_3 = \omega_1 + \omega_2. \quad (2.74)$$

As a nonlinear parametric process in which photons at different frequencies take part, the efficiency of FWM is highly depending on the phase matching condition, hence, deeply relying on the waveguide dispersion properties. Such required phase matching is more easily achieved if the second type of FWM is degenerated ($\omega_1 = \omega_2$), which is particularly interesting because a single frequency of the input laser can generate two new frequencies symmetrically with respect to the pump frequency. This case is usually addressed as

$$2\omega_p = \omega_s + \omega_{as} \quad (2.75)$$

where ω_p is the frequency of the pump, while ω_s and ω_{as} are, respectively, the low frequency sideband at the Stokes frequency and the high frequency sideband at the anti-Stokes frequency.⁷⁸ FWM can lead to significant spectral broadening when

waveguide operates in the anomalous dispersion regime and it is also relevant for supercontinuum generation.⁷⁸

2.4.4 Self-steepening

Higher order nonlinearities not addressed in the nonlinear Schrödinger equation in the form of Eq. 2.57 may have significant impact in the propagating pulse if its intensity reaches levels high enough to trigger them. Self-steepening is an important high order nonlinear effect that has its origin on the intensity dependence of the group velocity.⁷⁸ Since the central part of the pulse carries most of the pulse intensity, it experiences a higher group index and, consequently, lower group velocity compared with its edges. Figure 2.11(a) shows that as pulse propagates its central part moves towards the trailing edge, making it steeper. It results in an asymmetric spectrum generated by the induced SMP, as illustrated in Fig. 2.11(b), which presents more intensity in the downshifted frequencies but a noticeable larger broadening on the upshifted frequencies. Self-steepening is responsible for substantial spectral broadening of ultrashort pulses in nonlinear waveguides and can lead to optical shock.

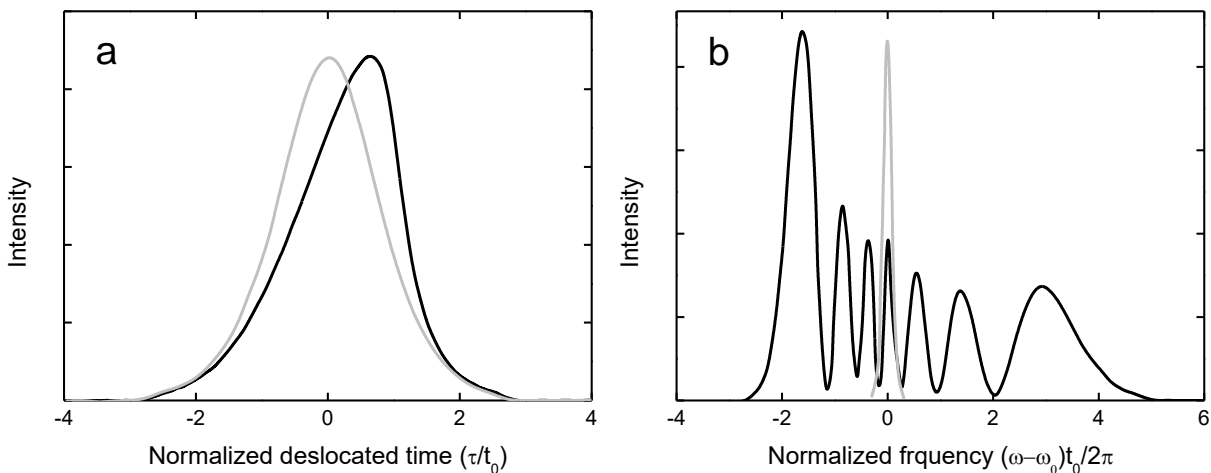


Figure 2.11 – (a) Self-steepening effect of a propagating optical pulse and (b) the asymmetric spectrum generated via self-phase modulation. In both graphs, the light gray line represents the pulse feature before propagation.

Source: Adapted from AGRAWAL.⁷⁸

2.4.5 Stimulated Raman scattering

In contrast to all previous mentioned nonlinear effects, Raman scattering is a nonparametric process in which the initial quantum state of the material is altered after

interacting with the optical field. Spontaneous Raman scattering is an inelastic scattering that involves energy transfer from an incident photon to a vibrational or rotational molecular system.⁸¹ Since energy and momentum must be conserved, if the material ends in a higher energy level, the photon is scattered with lower energy and it is classified as a Stoke scattering. The opposite case may also occurs and, in this case, the material ends in a lower energy level and the scattered photon has higher energy; such process is named anti-Stoke scattering. The combined action of stimulated emission and Raman scattering results in stimulated Raman scattering (SRS), which leads to Raman amplification. The Raman gain spectrum of a material gives the amount of photons scattered as function of the frequency shift and it is an expression of vibrational and rotational level systems of the material. Amorphous materials, such as silica, for example, present a rather continuous molecular motion configuration that produces a relatively large frequency shift range. Raman gain spectrum of silica pumped at 1 μm is shown in Fig. 2.12; it extends over 40 THz and has a maximum around 13 THz.⁷⁸

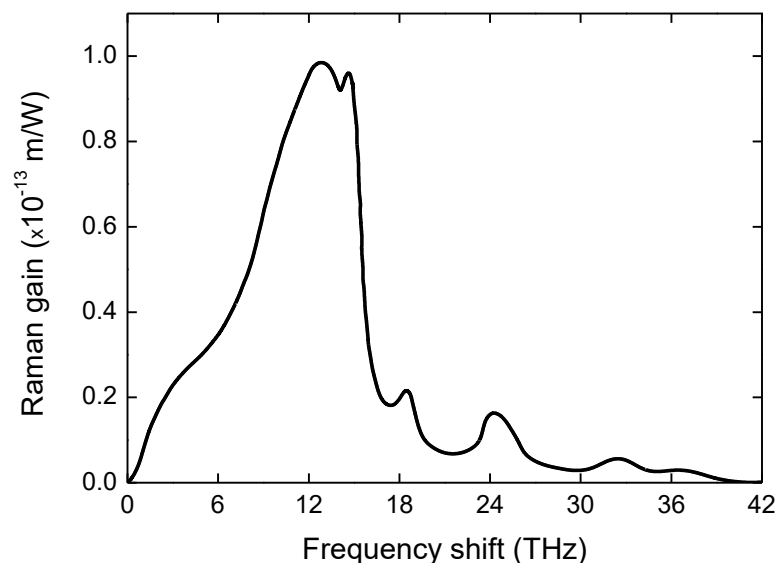


Figure 2.12 – Raman gain spectrum for fused silica pumped at 1 μm .
Source: Adapted from AGRAWAL.⁷⁸

SRS is a manifestation of the imaginary part of the third-order susceptibility that gives origin to the absorptive contribution of the nonlinear refractive index n_2 . In addition to spectral broadening due to generation and amplification of spectral components of high intensity pulses propagating in waveguides, SRS also is responsible for soliton self-frequency shift (SSFS) that is relevant for soliton dynamics in supercontinuum generation.⁸⁰

2.4.6 Supercontinuum generation

Supercontinuum generation (SCG) is a phenomenon that is the product of a combination of several nonlinear optical effects occurring simultaneously in the waveguide. Its complexity comes from the dependence on many characteristics of the waveguide, such as material, geometrical features and propagation length, and of the pump source, such as the guided intensity, wavelength and temporal width. The main nonlinear effects that participate on the SCG are self-phase modulation (SPM), cross-phase modulation (XPM), four-wave mixing (FWM), modulation instability (MI), soliton dynamics, self-steepening and stimulated Raman scattering (SRS).⁷⁹⁻⁸⁰

The dynamics of a supercontinuum generated from ultrashort pulse propagation can be divided in categories, according the dispersion regime in which the waveguide is operating. When the pump is in the anomalous dispersion regime, SPM allows the formation of optical solitons that undergo self-steepening and FWM, generating new spectral content. SRS shift solitons to longer wavelengths broadening the spectrum. Then, higher order solitons break due to SRS and high order dispersion, resulting in energy transfer to shorter wavelengths that have the same group index via a phase matched process called dispersive waves. On the other hand, when the pump is in the normal dispersion regime, there is no soliton formation and, therefore, SCG relies only on SPM and SRS to broaden the pulse spectrum.

3 EXPERIMENTAL

Chapter 3 covers the details of experimental setups used to measure sample nonlinearities, to inscribe waveguides and couple light in order to characterize their linear and nonlinear properties.

3.1 Z-scan and Optical Kerr-Gate

The third-order optical nonlinearities of glass samples, specifically the nonlinear absorption coefficient (β) and the nonlinear refractive index (n_2), were measured by the Z-scan technique. The nonlinear response time measurements were carried out using the Optical Kerr-Gate (OKG) technique. Both techniques were performed using 120-fs pulses at 1 kHz repetition rate and wavelength ranging from 460 nm to 1.5 μm , delivered by an Optical Parametric Amplifier (OPA) pumped by 150-fs pulses from a Ti:Sapphire amplifier, centered at 775 nm and operating at 1 kHz (Clark – MRX). Figure 3.1(a, b) display a schematic representation of the closed- and open-aperture Z-scan setup, in which measurements from the visible to the telecommunication range were performed with beam waist varying from 14 to 27 μm , guaranteeing that the beam confocal parameter was greater than the sample thickness, and pulse energy from 100 to 300 nJ, both depending on the selected wavelength. The signal was measured by a silicon or germanium photodetector, depending on the spectral region. The concept of both Z-scan configurations is to analyze the normalized transmittance of the sample while it is being translated along the laser propagation direction. In the open-aperture version, the entire transmitted beam is collected by the detector using a lens in order to evaluate if there was absorption originated by the imaginary part of the third order nonlinear susceptibility. In the closed-aperture version, an iris partially blocks the transmitted beam before hitting the detector to measure signal variation coming from refractive Kerr-optical lens effect produced by the real part of the induced nonlinearity. OKG experiments were performed in a setup illustrated in Fig. 3.1(c) at 520, 650 and 790 nm, also using the OPA as excitation source. It is a pump-probe technique that uses a pair of crossed polarizers and a delay stage to probe, at different moments, the birefringence produced by the nonlinear refractive index induced by the pump. More information can be found in references.⁸²⁻⁸³

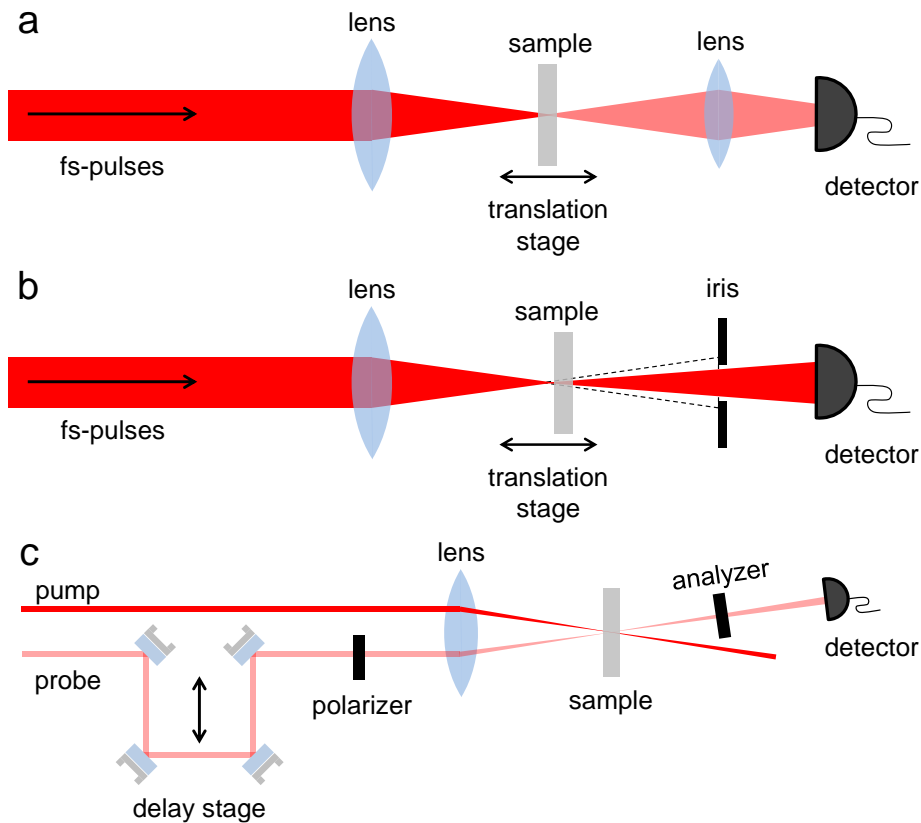


Figure 3.1 – Schematic of the experimental setup used for the (a) open- and (b) closed-aperture Z-scan and (c) Optical-Kerr Gate measurements.
Source: By the author.

3.2 Femtosecond laser writing

Femtosecond laser writing, surface ablation and waveguide inscription, were carried out in two different laser systems. Besides the amplified laser (150-fs, 1 kHz, 775 nm) described in Section 3.1, we also used an extended cavity Ti:Sapphire laser oscillator that delivers 50-fs pulses centered at 800 nm and operating at a repetition rate of 5 MHz (Femtosource – 100XL). The same micromachining setup was used with both laser systems and its illustration is shown in Fig. 3.2. The laser pulses have their energy set by a half-wave plate and a polarizer, and are focused by a microscope objective on the sample mounted on a computer controlled three-dimension translation stage that moves perpendicularly to the beam propagation direction (transverse configuration). The translation stage is composed by three microactuators (Thorlabs Z825B) with moving range of one inch, scan speed ranging from 1 up to 450 $\mu\text{m/s}$ and precision of 50 nm. Software developed, during this dissertation, in LabView[®] give freedom to position the sample in relation to the beam focus, allowing controlling fs-laser processing on the sample's surface or in a specific depth inside the bulk, as well

as to control the scanning speed. The micromachining process can be monitored in real time with the aid of a CCD camera and a backlight illumination.

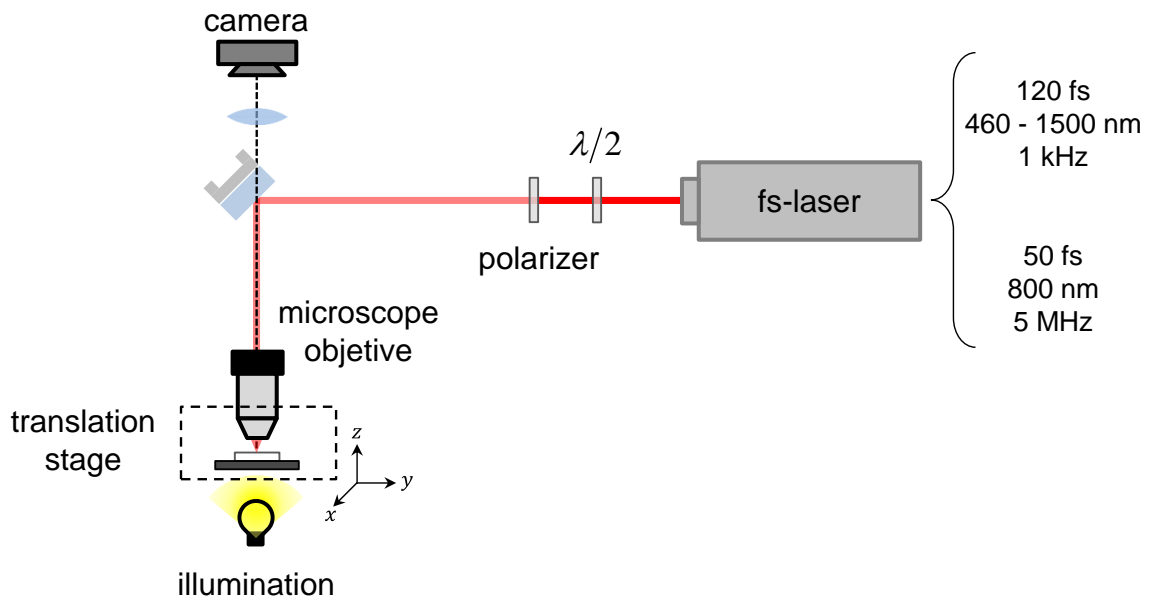


Figure 3.2 – Illustration of the femtosecond laser writing setup in the transverse configuration.
Source: By the author.

This fs-laser writing setup is a versatile tool for ultrafast processing a broad variety of materials, since it can be used changing the excitation wavelength, pulse energy, sample position, scanning speed and patterns.

3.3 Waveguide characterization coupling system

Femtosecond laser inscribed waveguides had their linear and nonlinear characterization performed in an objective-lens based coupling system. In this setup, as shown in Fig. 3.3, the laser beam is coupled into the waveguide by an input objective, which can have different numerical apertures, and the transmitted light is collected by an output objective. The intensity distributions of the guided modes within the waveguides were analyzed by projecting its images on a CCD camera. Losses were determined by transmittance measurements taken into account both objective transmission and Fresnel refractions. The measured transmittance loss α_{trans} is, in fact, a combination of losses from distinct sources categorized in coupling, α_{coupl} , and guiding, α_{guid} , losses that can be expressed as

$$\alpha_{trans} = \alpha_{coupl} + \alpha_{guid} \quad (3.1)$$

and each loss contribution can be obtained applying the traditional cutting method.^{84,85} However, as this method involves cutting the waveguide we decided to use instead a non-destructive method, in which the coupling loss is calculated from the mode mismatching⁸⁶⁻⁸⁷ between the input Gaussian laser beam and the guided mode given by

$$\alpha_{coupl} = -10 \log_{10} \left[\frac{(\iint E_g E_l^* dx dy)^2}{\iint E_g E_g^* dx dy \iint E_l E_l^* dx dy} \right] \quad (3.2)$$

where E_g and E_l are the field profiles of the guide mode and the input laser, respectively. Therefore, guiding loss is simply the subtraction of the calculated coupling loss from the measured transmittance loss.

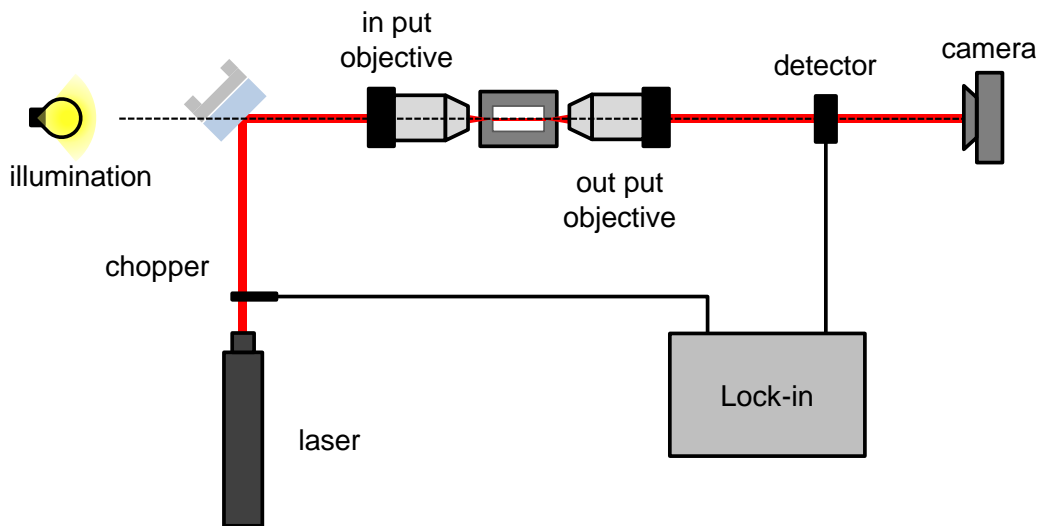


Figure 3.3 – Waveguide characterization coupling setup.
Source: By the author.

Optical alignment is critical for an efficient light coupling. The waveguide must be parallel to the laser beam propagation and its entrance and exit faces must be on the focal plane of the input and output objective lens, respectively. In order to satisfy these requirements, both objective lenses and sample positions are mounted on top of three-dimensional (x-y-z) precision stage.

Depending on the feature of the waveguide to be characterized and its materials, different lasers were used in the light coupling setup. Linear standard characterization was carried out using a He:Ne laser at 632.8 nm and a Ti:Sapphire laser at 800 nm (Femtosome – 100XL), operating in the continuous wave (cw) regime.

While nonlinear characterization was performed using femtosecond pulses from three distinct sources, in which two of them are the previously described Femtosource (50-fs, 5MHz, 800 nm) and Clark – MXR (150-fs, 1 kHz, 775 nm), and the third one is a laser system composed by an OPA emitting 50-fs pulses at 1 kHz repetition rate at tunable central wavelength, which is pumped by 50-fs pulses from a Ti:Sapphire multi-pass amplifier, centered at 780 nm, operating at 1 kHz (Dragon). Since the nonlinear effects observed in our experiments are related to new frequency generation processes, we adapted the setup displayed in Fig. 3.3 by replacing the detector by a spectrometer to analyze any changes in the guided spectrum.

4 THIRD-ORDER OPTICAL NONLINEARITIES IN BULK AND FS-LASER INSCRIBED WAVEGUIDE IN STRENGTHENED ALKALI ALUMINOSILICATE GLASS†

The development of advanced photonics devices requires materials with large optical nonlinearities, fast response times and high optical transparency, while at the same time allowing for micro/nano-processing needed for integrated photonics. In this context, glasses have been receiving considerable attention given their relevant optical properties which can be specifically tailored by compositional control. Corning Gorilla® Glass (strengthened alkali aluminosilicate glass) is well-known for its use as protective layers in mobile devices, and has attracted interest as a potential candidate for optical devices. Therefore, it is crucial not only to expand the knowledge on the fabrication of waveguides in Gorilla Glass under different regimes, but also to determine its nonlinear optical response, both using fs-laser pulses. Thus, this chapter reports the characterization of third-order optical nonlinearities of Gorilla Glass, for the first time, as well as linear and nonlinear characterization of waveguides written with femtosecond pulses under the low repetition rate regime (1 kHz).

4.1 Bulk nonlinearities of Gorilla® Glass

Gorilla Glass third-order optical nonlinearities were initially measured using closed-aperture Z-scan technique, as described in Section 3.1 of Chapter 3, from the visible to the telecommunication range. The studied spectral range covers most of its transparency window as showed in the absorbance spectrum presented in the left inset of Fig. 4.1. As can be seen in Fig 4.1, the determined n_2 value is approximately constant in the studied spectral region (490 – 1500 nm), with a mean value of $(3.3 \pm 0.6) \times 10^{-20} \text{ m}^2/\text{W}$. Such result show that Gorilla Glass exhibits a nonlinear index of refraction higher than fused silica, a material commonly used for comparison purposes, where n_2 is $(2.5 \pm 0.2) \times 10^{-20} \text{ m}^2/\text{W}$ at around $1 \mu\text{m}$.⁸⁹ Specifically at $1 \mu\text{m}$, we obtained for Gorilla Glass an n_2 value of $(3.4 \pm 0.6) \times 10^{-20} \text{ m}^2/\text{W}$. Such result is in agreement with the nonlinear refractive index obtained for alkaline glasses reported in the literature, whose values range from 2.2 to $3.4 \times 10^{-20} \text{ m}^2/\text{W}$. The right inset in Fig. 4.1 is a Z-scan signature measured at 810 nm.

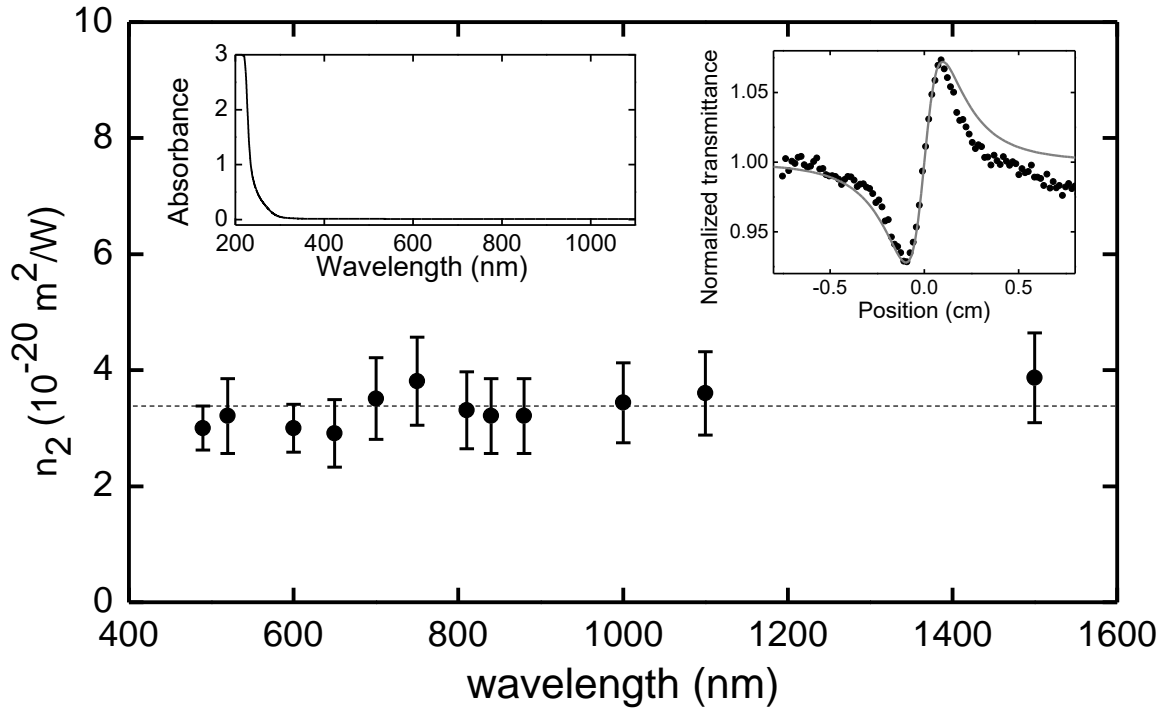


Figure 4.1 – Nonlinear refractive index of Gorilla Glass obtained by Z-scan measurements. The dashed line is the average value of $3.3 \times 10^{-20} \text{ m}^2/\text{W}$. The left inset shows the absorbance spectrum of Gorilla Glass and the right inset displays the experimental (black dots) and theoretical (gray curve) Z-scan signature trace at 810 nm.
Source: Adapted from ALMEIDA.⁸⁸

As it is known, Gorilla Glass is strengthened via ion exchange, which results in the formation of a compression layer that extends about $150 \mu\text{m}$ below the surface. Therefore, since Z-scan measurements (Fig. 4.1) were carried out in the thin-sample regime, the measured nonlinear refractive indexes are, in fact, effective values that take into account the two compressed layers (on both sides of the sample) and the untreated layer (in the center) that comprise our sample (total thickness of $700 \mu\text{m}$). In such case, the total induced nonlinear phase is given by the sum of the nonlinear phases for each layer. Although the ion exchange process alters the glass composition and the mechanical properties of the compression layers, our results indicate that the nonlinear optical properties are not significantly affected, once the effective n_2 measured is very similar to the ones reported for the same class of glass⁹⁰⁻⁹¹, i.e. the nonlinear response of the compression (strengthened) layer is similar to that of the untreated region, within the experimental error. If that was not the case, an appreciable difference (outside the experimental error) would be observed. It is also interesting to point out that nonlinear absorption signal was not observed in open-aperture Z-scan measurements over the spectral region and intensity levels of approximately $100 \text{ GW}/\text{cm}^2$ used in the experiments.

The response time of the nonlinear optical effect was determined by the OKG technique presented in Section 3.1, which was performed at 520, 650 and 790 nm. The OKG signals obtained at each wavelength are shown in Fig. 4.2 and correspond to response times of 250, 165 and 170 fs (Full Width Half Maximum) that is in the same order of the excitation pulse temporal width, indicating that the sample's nonlinear process is faster than the pulse itself and it can be characterized as an ultrafast electronic process.

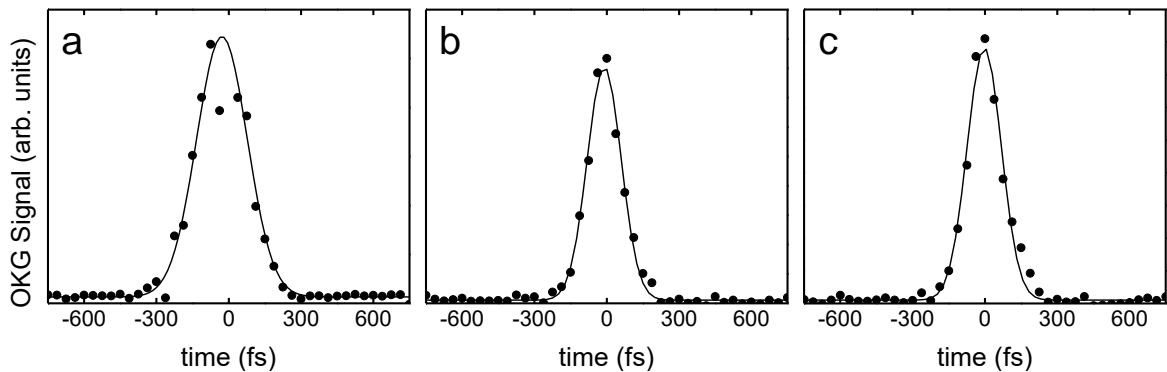


Figure 4.2 – OKG signal of Gorilla Glass at (a) 520, (b) 650 and (c) 790 nm.
Source: By the author.

4.2 Femtosecond laser micromachining and waveguide inscription

Given the Gorilla Glass bulk nonlinearities, we inscribed waveguides into it using femtosecond pulses to evaluate its potential for photonic devices. In order to do that, we first studied the ultrafast laser micromachining process of Gorilla Glass by using the femtosecond laser writing setup detailed in Section 3.2. In this experiment the beam was focused by a microscope objective with numerical aperture $NA = 0.65$ on the sample, mounted on a computer controlled x - y - z stage. The influence of excitation wavelength, pulse energy, and scanning speed was investigated by producing a series of grooves onto sample surface. Ablated grooves were microfabricated by pulses at 520, 650 and 775 nm at scanning speeds of 50, 200 and 400 $\mu\text{m/s}$ with energy ranging from 500 nJ up to 16 μJ and were analyzed by optical microscopy. As an example, in Fig. 4.3 are displayed the optical images of micromachined grooves at the surface of Gorilla Glass using pulses centered at 520 nm at 50 $\mu\text{m/s}$ with several pulse energies.

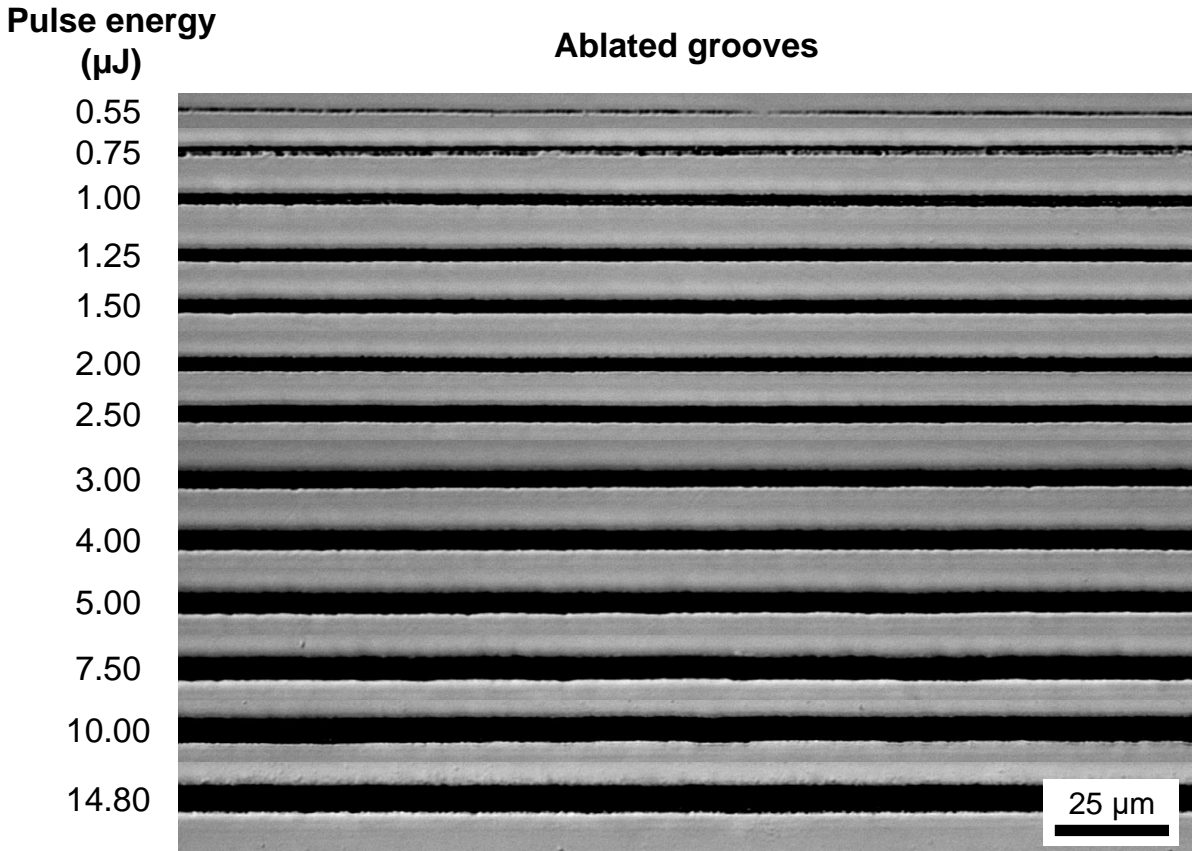


Figure 4.3 – Optical microscopy images from ablated grooves at Gorilla Glass surface using fs-laser pulses centered at 520 nm at scanning speed of 50 $\mu\text{m/s}$ as function of pulse energy.
Source: By the author.

Groove width measured as a function of the fabrication pulse energy revealed a logarithmic behavior predicted by the expression $r_{th}^2 = (w_0^2/2) \ln(E/E_{th})$, presented in Eq. 2.34, as can be seen in Fig. 4.4(a, b, c) that presents the experimental data for a Gorilla Glass sample micromachining with pulses at 520, 650 and 775 nm at three different scan speeds. From the angular coefficients of the fitting curves (black, light gray and dashed lines) we could determine the beam waist for each excitation wavelength of $(1.9 \pm 0.2) \mu\text{m}$, $(2.2 \pm 0.2) \mu\text{m}$ and $(1.9 \pm 0.2) \mu\text{m}$, respectively, and the energy threshold for each case was obtained by the point in which the fitting curves crossed the abscissa axis. The energies for ablation threshold under distinct scan speeds and excitation wavelengths are shown in Fig. 4.4(d). Such results show an approximately constant behavior around 475 nJ, revealing that fs-laser micromachining of Gorilla Glass is wavelength independent. The Keldysh parameter ($\gamma_K = \omega_0/\Omega_{tun}$) that describe the ionization picture is the ratio between the excitation light frequency and the tunneling “frequency”, that depends on the electron charge, effective mass, material energy gap and light electric field. For all wavelengths and

pulse energies used in this work the Keldysh parameter is smaller than 0.3, which indicates that photo-ionization is governed by tunneling rather than multiphoton absorption, corroborating the results presented in Fig. 4.4(d).

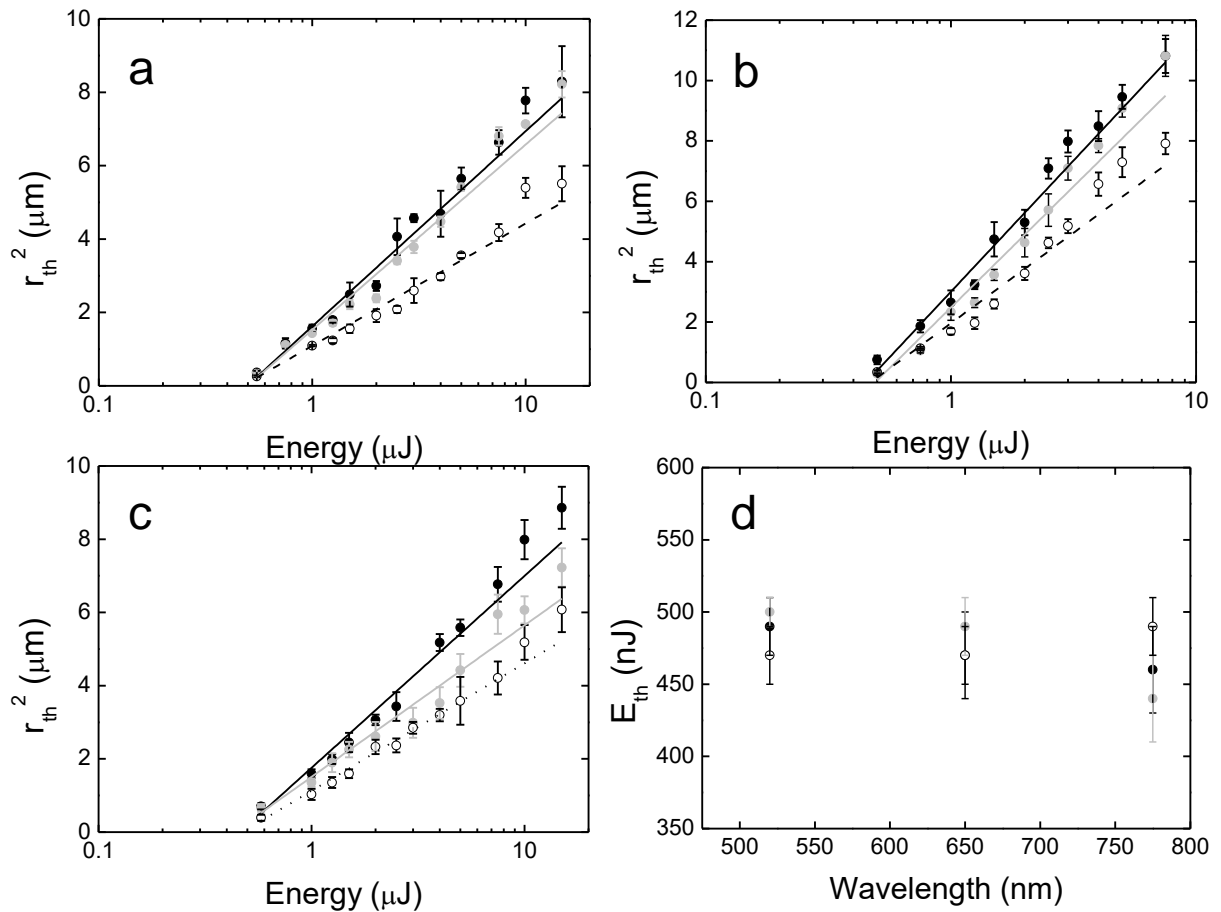


Figure 4.4 – Squared groove radii (r_{th}^2) as function of the pulse energy at (a) 520, (b) 650 and (c) 775 nm for scanning speeds of (\bullet) 50, (\circ) 200 and (\circ) 400 $\mu\text{m/s}$. The lines correspond to the fitting obtained with the expression given in the text. (b) Threshold energy (E_{th}) as a function of excitation wavelength for each scanning speeds.

Source: By the author.

With the micromachining parameters determined, the inscription of 15-mm long waveguides was carried out in the same femtosecond laser writing setup by placing the beam focus 100 μm inside the glass, with sample scanning speed of 200 $\mu\text{m/s}$, using pulses centered at 775 nm and energies of 250 nJ, 1 and 5 μJ . After polishing the sample faces, waveguides longitudinal and transversal profiles were evaluated via optical microscope images.

4.3 Linear and nonlinear characterization of fs-inscribed waveguides

For linear and nonlinear characterization of inscribed waveguides, we used the light coupling setup presented in Section 3.3, in which the numerical aperture of the input and output objectives was $NA = 0.25$ and $NA = 0.65$, respectively. Two lasers were used as light sources, a *cw* He-Ne laser at 632.8 nm and a Ti:Sapphire amplified laser (Clark – MXR) emitting 150-fs pulses, centered at 775 nm and operating at 1 kHz. The produced waveguides can be classified regarding its fabrication pulse energy with respect to the energy threshold of ~ 475 nJ. For the waveguides inscribed with 250 nJ pulses (lower than the ablation threshold), Fig. 4.5 displays its narrow (a) longitudinal and symmetrical (b) transversal profiles. The intensity distribution shown in Fig. 4.5 represents the guided modes obtained at (c) 632.8 and (d) 775 nm, respectively, both exhibiting singles mode guiding, probably due to the small waveguide diameter, as well as the smooth refractive index change induced during the fs-laser processing.

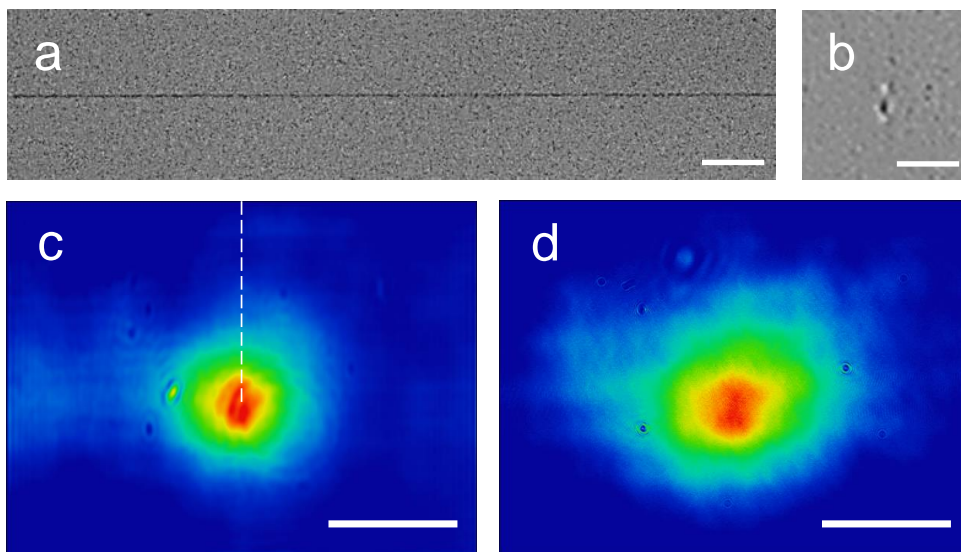


Figure 4.5 – Microscope images of (a) longitudinal and (b) transversal profiles of waveguides fabricated with pulse energy of 250 nJ and its guided mode intensity distribution obtained for coupling light at (c) 632.8 and (d) 775 nm. Scale bar in each image corresponds to 10 μm .

Source: Adapted from ALMEIDA.⁸⁸

Waveguides produced with pulses energies higher than the ablation threshold energy also had their guiding modes characterized. Fig. 4.6 shows the transversal profiles for waveguides inscribed with pulse energies of 1.0 μJ and 5.0 μJ . The elliptical and elongated shape of their cross-section is attributed, respectively, to the perpendicular writing geometry and self-focusing.⁹² Although both factors are present

when writing waveguides with lower pulse energy, they have greater impact on waveguides fabricated with high pulse energies. The more complex intensity distributions of the guided modes displayed in Fig. 4.6 indicate higher order and/or multi-mode propagation, both at 632.8 and 775 nm, which is related to the large waveguide diameter and the spatial refractive index profile formed by negative variations in the center, due to material expansion (void) and positive variations due to material compression in the vicinities of the irradiated area. However, as for many applications it is rather preferred that the waveguide operates in the mono-mode regime, we continued our studies on the waveguides inscribed with 250 nJ (lower than the threshold energy).

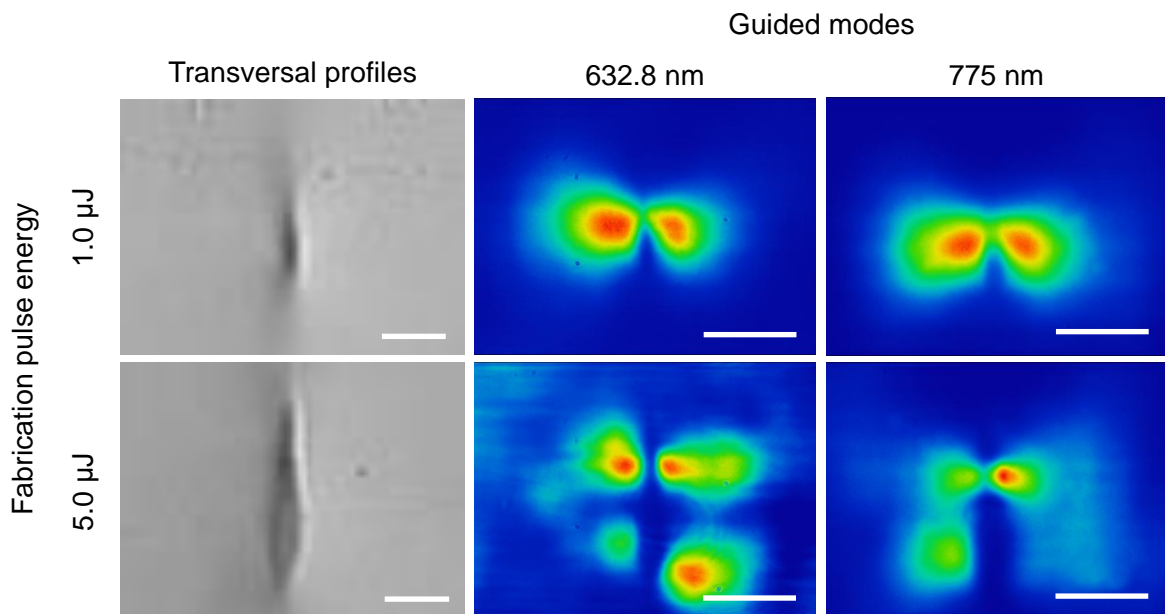


Figure 4.6 – Microscope images of transversal profiles of waveguides fabricated with pulse energies of 1.0 and 5.0 μJ and its corresponding guided mode intensity distributions, for light at 632.8 and 775 nm. Scale bar in each image corresponds to 10 μm .

Source: By the author.

Since the waveguides inscribed with energy lower than the ablation threshold (250 nJ) presented guided profiles that correspond to the fundamental mode, we used the analytical solution developed in Section 2.4.1 of Chapter 2, considering a step-index waveguide structure, to fit the experimental data in order to obtain other waveguide characteristics, as numerical aperture and refractive index variation. From the theoretical analysis, it is known that the mode amplitude is described by a Bessel function of the first kind $J_0(k_t r)$ for spatial coordinate in the core ($r \leq a$) and by a modified Bessel function of the first kind $K_0(\gamma r)$ for the spatial coordinate in the cladding ($r > a$). The boundary condition implies that these functions and its

derivatives must be continuous at the core-cladding interface ($r = a$). Thus, function continuity is achieved only if the amplitudes of the Bessel functions and its parameters k_t and γ are chosen correctly.

With the purpose of determining the best parameters to fit the experimental data, we selected the radial mode profile indicated by the white dashed line in Fig. 4.5(c). The procedure applied consists on dividing the experimental data in two parts at different radial distances r_0 , representing the core and cladding regions, fitting the inner part with $J_0(k_t r)$ and the outer part with $K_0(\gamma r)$, and then calculating the module of the difference of both derivatives. This procedure is graphically presented in Fig. 4.7(a), where the gray line represents a linear fitting of the left side of the plot to find an accurate radii value in which both fitted Bessel function derivatives are continuous. In Fig. 4.7(b), is shown the experimental data (black dots) fitted with the expression for the core (light gray curve) and the cladding (dark gray curve)

$$A(r) = \begin{cases} J_0(k_t r), & r \leq a \\ bK_0(\gamma r), & r > a \end{cases} \quad (4.1)$$

where $b = 0.699$ ensures amplitude continuity, Bessel parameters are $k_t = 0.503 \mu\text{m}^{-1}$ and $\gamma = 0.201 \mu\text{m}^{-1}$ and radii $a = 2.36 \mu\text{m}$. Furthermore, the good agreement between experimental results and analytical solution indicates that fs-laser inscribed waveguides present an index profile that can be well described by a step-refractive index waveguide.

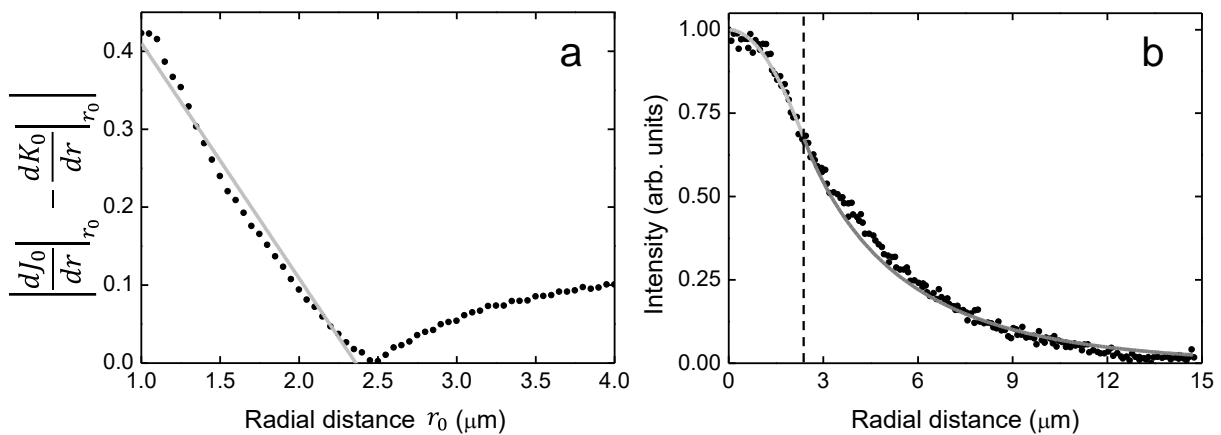


Figure 4.7 – (a) Determination of the Bessel function parameters (k_t and γ) and waveguide core radius from the derivative continuity boundary condition, and (b) experimental radial profile data (black dots) fitted by the core (light gray curve) and cladding (dark gray curve) expressions.

Source: By the author.

Recalling Eqs. 2.37 and 2.47 from Section 2.4.1, we have that

$$NA = \frac{\lambda}{2\pi} \sqrt{k_t^2 + \gamma^2} = \sqrt{n_1^2 - n_2^2} \quad (4.2)$$

and by assuming that the index of refraction of Gorilla Glass at 632.8 nm is 1.46, we determined the waveguide numerical aperture and core-cladding refractive index difference of 0.13 and 5×10^{-3} , respectively. Similar values have been reported for waveguide written with ultrashort pulses.⁹³ The performance of the waveguides was evaluated in both wavelengths used in the light coupling setup. Transmission measurements and calculated mismatch coefficients revealed guiding losses at 632.8 and 775 nm of 0.19 ± 0.01 dB/mm and 0.35 ± 0.01 dB/mm, respectively.

In order to study optical nonlinearities on the single-mode inscribed waveguides, 150-fs pulses at 775 were coupled into 15 mm long waveguides using a microscope objective with $NA = 0.25$, which is smaller than the one employed for waveguide inscription, in such way that the waveguides are not damaged in this experiments. Using the coupling setup we were able to obtain single mode guiding, similar to the one presented in Fig. 4.5(d). The pulse spectra at the waveguide input and output were measured using a spectrometer added to the coupling system. For low input pulse energy (coupled energy smaller than 120 nJ), no changes in the spectra bandwidth were observed in the output spectrum (spectrum similar to the gray line shown in Fig. 4.8(a)). However, when a pulse energy of 260 nJ is coupled to the waveguide, a broadened spectrum is observed at the output, generated by nonlinear optical effects induced by higher input pulse energies. The spectral broadening at the output is visualized in Fig. 4.8(a) (black) and can be compared to the input spectrum (gray). Such spectral broadening is assigned to self-phase modulation, as indicated by its symmetry and the presence of the characteristic self-phase modulation side peaks observed in Fig. 4.8(a).⁹⁴ Figure 4.8(b) shows the wider spectral broadening (black) achieved with input pulses of 380 nJ, which is compatible with the n_2 value determined by the Z-scan measurements. The gray line in this figure displays the transmittance of the filter used to block part of the intense 775 nm fs-pulse employed. The white light continuum (WLC) generated (450 – 800 nm) is again attributed to self-phase modulation, stimulated Raman scattering and higher order nonlinear phenomena.⁹⁵ An image of the guided mode is presented as an inset in Fig. 4.8(b), showing that the WLC

intensity distribution is rather homogeneous. As expected, the waveguide performance is not altered by the WLC generation experiments, under the conditions employed here.

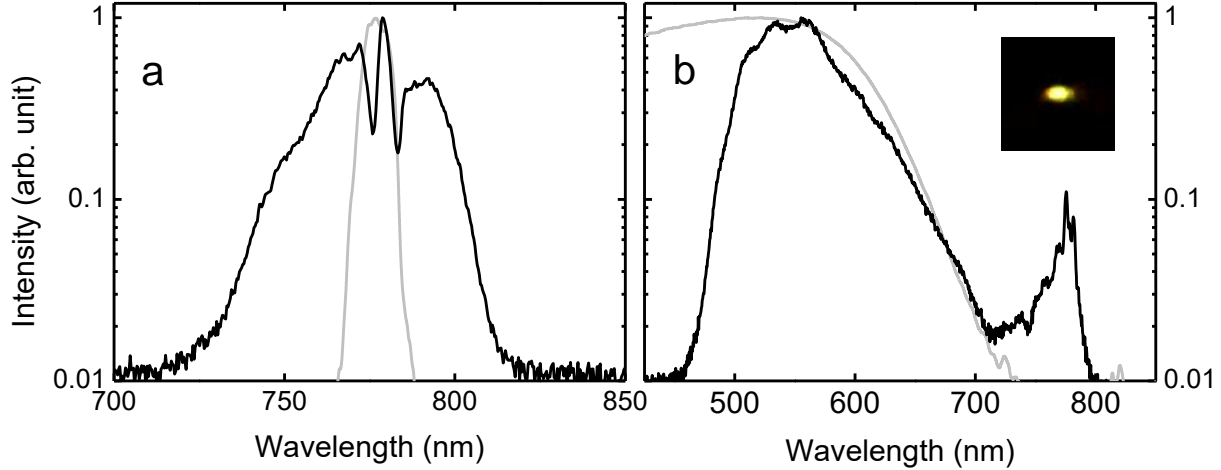


Figure 4.8 – (a) 260 nJ input pulses spectrum (gray) and its corresponding spectral broadening after propagation in 15-mm long waveguide. (b) Spectrum of the white-light (black) generated by a 380 μ J input pulse. The gray line displays the transmission of a filter used to attenuate fundamental pulse spectrum. The inset represents a colored image of the corresponding output guided mode.

Source: ALMEIDA.⁸⁸

Previous studies have reported spectral broadening and WLC generation resulting from ultrashort pulse propagation in tapered fibers.⁹⁶ Such studies have shown a trade-off between dispersion and nonlinearities during pulse propagation. The length scale for dispersion effects to become relevant, called dispersion length, is defined as $L_D = -t_0^2 2\pi c / (\lambda^2 D)$, in which t_0 is the pulse temporal width (150-fs), λ is the wavelength (775 nm), c is the speed of light, and D is the dispersion coefficient. Given that the refractive index change in fs-laser inscribed waveguides is on the order of 10^{-3} , its guiding properties can be interpreted in the weakly guiding regime⁹⁷, which leads to $D = -100$ fs/(nm·m) for the waveguides produced here. In this way, the fs-laser inscribed waveguides yield an $L_D \approx 1$ m and operate on the normal dispersion regime ($D < 0$). Similarly, the length scale regarding nonlinear optical effects, called nonlinear length, is $L_{NL} = t_0 / (\gamma E_0)$. The nonlinear optical parameter $\gamma = 2\pi n_2 / (\lambda A_{eff})$ depends on the nonlinear refractive index n_2 , measured by the Z-scan technique (Fig. 4.1) and on the effective area, A_{eff} , of the modal distribution, obtained from the results presented in Fig. 4.5(d). Estimating the coupled energy inside the waveguide as $E_0 \approx 200$ nJ, by evaluating the coupling losses, and using the laser parameters, as pulse duration and wavelength (150 fs and 775 nm), a nonlinear length of $L_{NL} \approx 2$ mm is obtained. Since

the calculated dispersion length ($L_D \approx 1$ m) is much longer the waveguide interaction length (15 mm), dispersion effects are not significant during pulse propagation. On the other hand, nonlinear optical effect manifested here through spectral broadening and white light continuum generation, are expected to be observed because the nonlinear length is smaller than the waveguide length.

4.4 Partial conclusion

The optical nonlinearities, magnitude and time response, of bulk Gorilla Glass and the performance of fs-laser inscribed waveguides have been evaluated in the femtosecond pulses regime. Z-scan measurements revealed that the effective nonlinear index of refraction measured shows to have a constant value of $3.3 \pm 0.6 \times 10^{-20}$ m²/W for wavelengths ranging from 490 nm up to 1500 nm (VIS-NIR region). Such nonlinearity is responsible for generating both, white-light and spectral broadening in waveguides written using 250 nJ femtosecond pulses. The analysis of guiding modes, dispersion and nonlinear optical effect in such waveguides revealed that Gorilla Glass presents a performance comparable to other glasses, being useful for the development of integrated nonlinear optical platforms.

5 NONLINEAR OPTICAL WAVEGUIDES INSCRIBED BY FS-LASER IN ORGANIC CRYSTAL FOR BROADBAND SECOND HARMONIC GENERATION OF UV PULSES

Optical waveguides are main components for the development of integrated photonics, not only for allowing light confinement and propagation control but also for their ability to act as nonlinear optical elements. Under specific conditions, such confinement gets tight enough to achieve very high intensities, favoring nonlinear optical processes to take place. Although nonlinear optical effects are detrimental for some waveguides applications, the correct design of devices to support specific nonlinear optical effects are of great promise for the future of full-optical signal processing. Direct laser writing with ultrashort pulses has provided considerable advances in the fabrication of 3D waveguides and the improvement of its optical properties. Nonetheless, such progresses have been achieved for waveguides designed in inorganic materials and little attention has been devoted to organic crystals, which offer new perspectives for the field. Amino acid based organic crystals are interesting nonlinear optical materials that exhibit high second order nonlinear properties^{50,98}, therefore, can be used for second harmonic generation (SHG), optical parametric amplification (OPA) and optical parametric oscillation (OPO).⁹⁹ In this context, Chapter 5 reports the inscription of circular cross-section cladding waveguides by fs-laser in organic L-threonine crystals and its linear and nonlinear optical characterization. Guided broadband ultra-violet (UV) second harmonic light was demonstrated. Interestingly, inscribed waveguides presented higher second harmonic generation efficiency when compared to the crystal itself, which was assigned to the influence of the waveguide dispersion contribution to the phase-matching condition.

5.1 Cladding waveguide structure

Volumetric modification of transparent media by tightly focused ultrashort pulses is only possible due to the fact that its absorption is ruled by intensity-dependent nonlinear interactions, which restricts it to the beam focal volume. The ability of spatially selecting the change in the material's optical properties makes femtosecond laser a highly suitable tool for the inscription of three-dimensional structures capable of guiding light in different types of materials.^{37,100-101} As illustrated in Fig. 5.1, laser-

inscribed waveguide structures can be divided into three main categories regarding the resulting refractive index change.³⁷

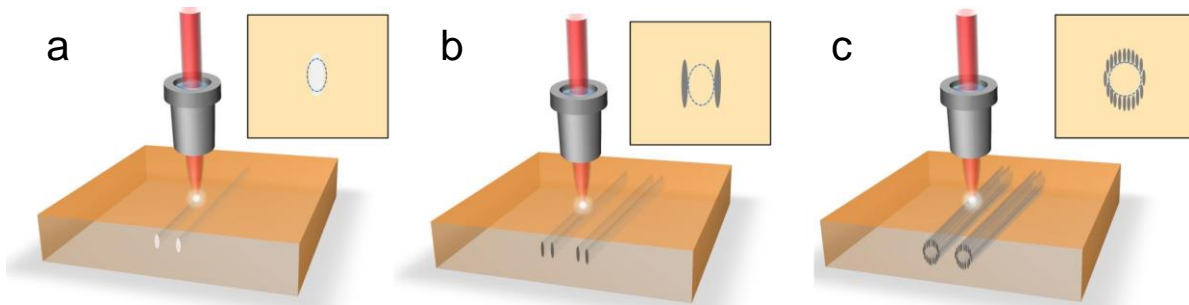


Figure 5.1 – Illustration of (a) type I, (b) type II and (c) type III configurations of waveguides inscribed in transparent material and its respective transversal profiles.
Source: Adapted from CHEN.³⁷

Type I is the most common waveguide produced and refers to the case in which the irradiated area exhibits an increase in the refractive index, allowing light to be guided within the modified region. Type II, also called as double-line, is assigned to a waveguide composed by two inscribed tracks that present a negative index change in its center, due to material's expansion and stress-induced positive changes in the vicinities. In such structure, light is guided in between the tracks. Finally, a type III waveguide consists of a number of very close tracks with a negative index change forming a lower refractive index contour acting as a cladding for a higher index core, thus receiving the name of cladding waveguide.¹⁰² Since light is guided where material hasn't been modified, it is extremely suitable for crystalline materials whose structural properties are relevant to the final purpose of the device.

5.2 L-threonine crystal and experimental setup

L-threonine (threo- α -amino- β -hydroxy- η -butyric acid) is an organic amino acid with the chemical formula $C_4H_9NO_3$ ¹⁰³, whose crystalline form presents an orthorhombic structure with the space group symmetry $P2_12_12_1$.¹⁰⁴ For this work, good optical quality L-threonine crystals were obtained by the slow evaporation method at constant temperature (20° C), using as a seed a crystal cut perpendicularly to the z-axis, known as the one that exhibits the highest growth rate. As seen in Fig. 5.2, such biaxial crystals present a wide transparency window, ranging from 250 up to 1500 nm, and its optical axis exhibit low refractive index of about 1.5 – 1.6 in the visible range.⁵⁰ The grown L-threonine crystals were cut, lapped and polished with final dimensions of

(5.5×7×9.3) mm³. To achieve phase-matched second harmonic generation (SHG) at 742 nm (second harmonic at 341 nm), the crystal was prepared such that the fundamental beam incidence is normal to one of its surfaces.

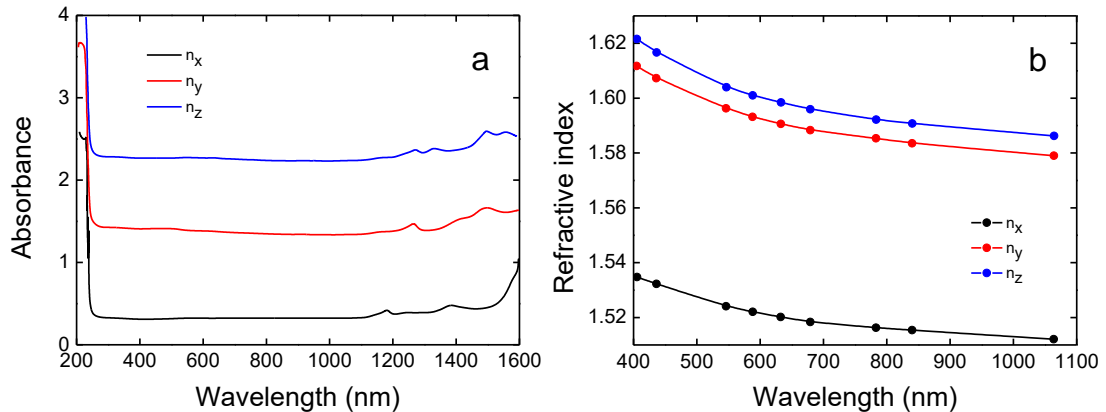


Figure 5.2 – (a) Absorbance spectra of a 1.5 mm-thick L-threonine crystal for light polarized parallel to the principal axes. Curves for y and z axes are vertically shifted. (b) L-threonine refractive index dispersion.

Source: Adapted from RODRIGUES JR.⁵⁰

The waveguides were inscribed by using an extended-cavity Ti:Sapphire laser oscillator, which delivers 50-fs pulses centered at 800 nm, operating at a 5 MHz repetition rate. Such laser delivers pulses with a maximum energy of 100 nJ, that was attenuated by a half-wave plate and a polarizer to control the pulse energy during the direct-laser writing. Pulses were tightly focused by a microscope objective (0.4 numerical aperture) 100 μ m beneath the sample surface, which was placed on a computer-controlled three-axis translation stage. The modification induced by the laser within the sample was monitored in real time with the aid of a backlight illumination and a CCD camera. Preliminary inscription tests were performed using different scan speeds and pulse energies in order to determine optimal parameters for the production of cladding waveguides. Its longitudinal and transversal profiles were evaluated by optical microscopy. Waveguide transmission losses and guided modes were characterized in an objective lens based coupling system, using cw light at 632.8 nm and 800 nm, from a He-Ne and a Ti:Sapphire laser, respectively. A set of five microscope objectives with a numerical aperture (NA) ranging from 0.1 up to 0.65 was used to couple light into the waveguide, while a fixed objective with NA = 0.4 was used to collect the guided light at the waveguide output. To investigate the second harmonic generation of broadband ultra-violet femtosecond pulses in the L-threonine crystal inscribed waveguide, a Ti:sapphire multi-pass laser amplifier (1 kHz) emitting 50-fs

pulses (780 nm) with 25 nm of Full Width at Half Maximum (FWHM) was used to pump an Optical Parametric Amplifier (OPA), which delivers 50-fs pulses with tunable central wavelength. Such laser system was used with the coupling setup to measure the waveguide nonlinear properties.

5.3 Waveguide fs-laser inscription, linear and nonlinear characterization

Initially, we studied the experimental conditions for waveguide inscription into the L-threonine crystal by writing several waveguides, varying pulse energy and scan speed. From such experiments, we determined the optimal parameters as 50 $\mu\text{m/s}$ and 14 nJ. Figure 5.3 shows optical microscope images from the longitudinal (a) and transversal (b) profiles of a waveguide inscribed 100 μm beneath the sample surface. As usually observed for fs-laser micromachining in crystals, we did not see guiding in such structures, indicating a laser-induced decrease in the refractive index of the sample.^{37,105}

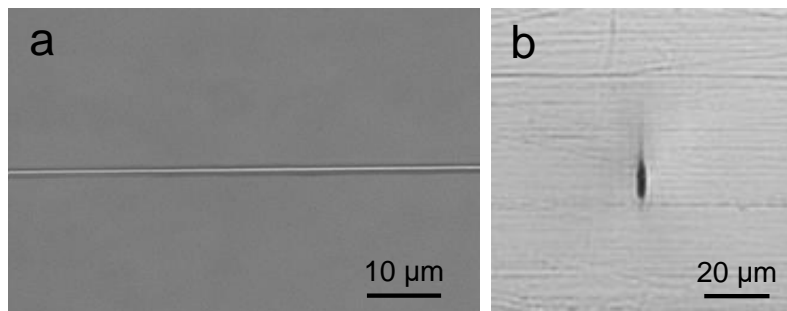


Figure 5.3 – Longitudinal (a) and transversal (b) optical microscope images of inscribed waveguide.
Source: By the author.

Since the interaction between fs-laser pulses and the crystal leads to a decrease in the refractive index of the irradiated regions due to material expansion, we inscribed waveguides separated by 20 μm to take advantage of the stress-induced increased refractive index surrounding central region. In Fig. 5.4 is shown the (a) longitudinal and (b) transversal profiles of the double-line waveguide, and its (c) guided mode intensity distribution at 632.8 nm. Guidance was only observed between the inscribed tracks that presented the proper refractive index contrast.

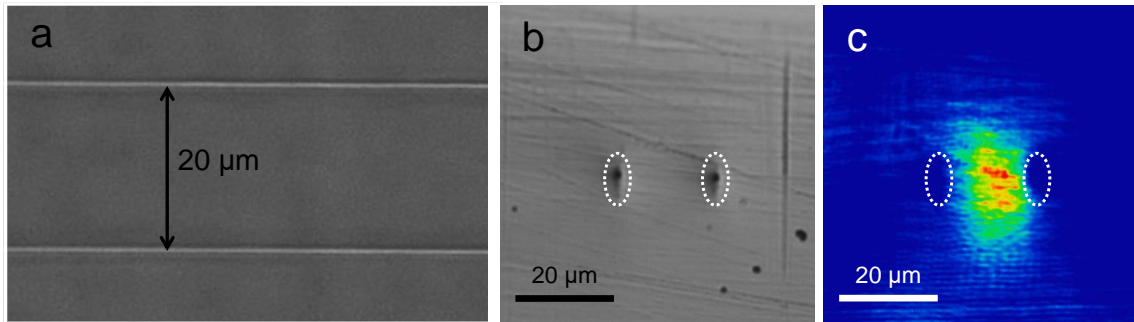


Figure 5.4 – Double-line inscribed waveguides (a) longitudinal and (b) transversal optical microscope images, and its (c) guided mode intensity profile at 632.8 nm.
Source: By the author.

With better understanding of the refractive index profile induced by the fs-pulse in L-threonine crystals, closed cladding waveguide structures can be produced, which would not only provide greater light confinement but also allow guidance in a region where the material's optical properties remain unaffected from laser modifications. Therefore, we inscribed 5.5 mm-long cladding waveguides 100 μm below the crystal surface, which are composed of 20 tracks creating a circular cross-section of 55 μm of diameter. Figure 5.5 shows a (a) 3D schematic representation of the cladding waveguide, as well as optical microscope images of the fabricated waveguide's (b) transversal and (c) longitudinal profiles.

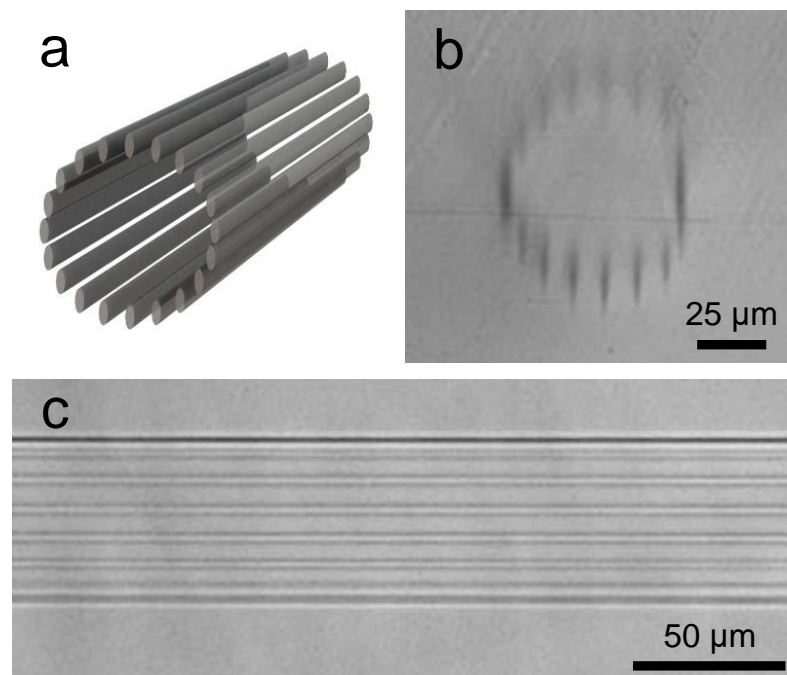


Figure 5.5 – (a) Three-dimensional scheme of the inscribed cladding waveguide and microscope images of its (b) transversal and (c) longitudinal profiles.
Source: By the author.

The characterization of the produced cladding waveguides was performed by coupling *cw* laser light at 632.8 nm and 800 nm using microscope objectives with different numerical apertures (NA). As seen in Fig. 5.6, a significant increase in the waveguide transmission is observed when lower NAs are used, for both wavelengths. Such result indicate that the inscribed waveguides present an NA smaller than 0.1, from which we can estimate the refractive index difference between the core and the cladding as being smaller than $\sim 2 \times 10^{-3}$, in agreement with cladding waveguide structures reported in the literature.^{100-101,106}

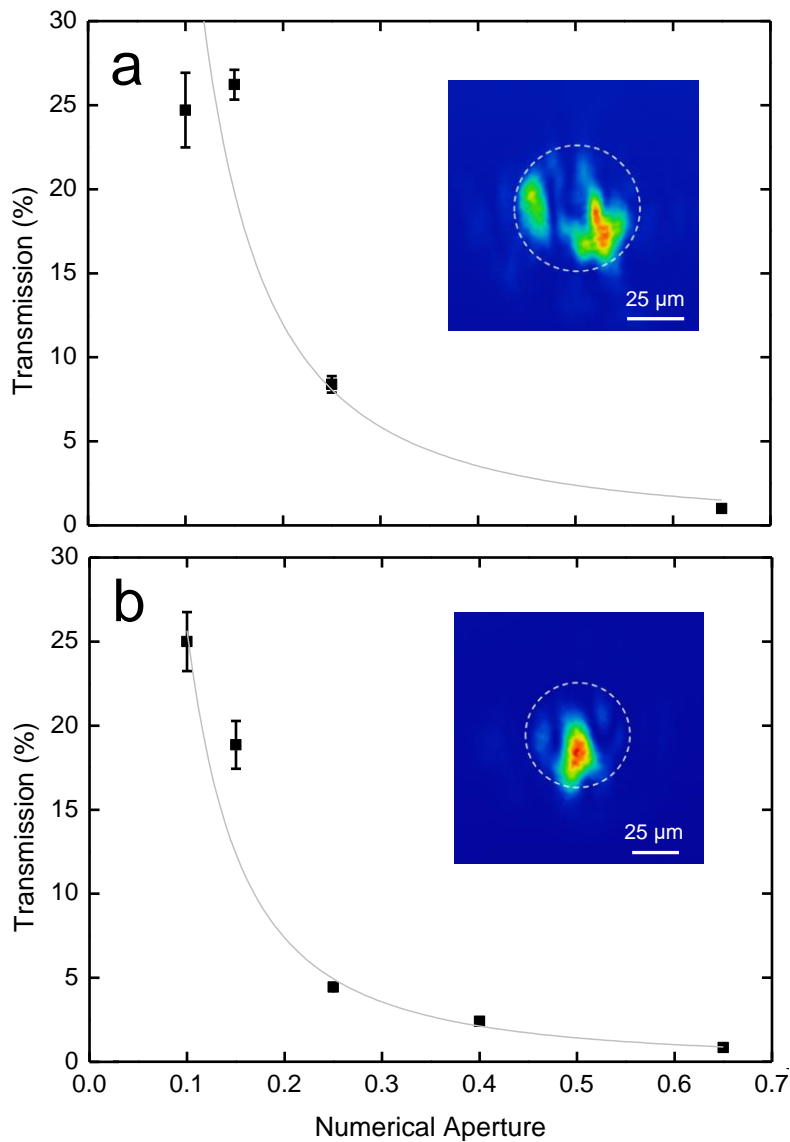


Figure 5.6 – fs-laser inscribed cladding waveguide transmission as function of the input numerical aperture lens for *cw* laser at the wavelengths of (a) 632.8 nm and (b) 800 nm. Its correspondent guided mode intensity distributions for an input NA of 0.1 are shown in the insets.

Source: By the author.

The insets in Fig. 5.6 (a) and (b) represent the guided mode intensity distributions at 632.8 nm and 800 nm, respectively, obtained using a coupling objective with NA=0.1. In both cases, the distribution indicates guiding under multimode conditions. From such guided modes, we calculated the mismatch coefficients, which corresponds to the fraction of light coupled into the waveguide, obtaining coupling losses of (3.9 ± 0.1) dB at 632.8 nm and (3.5 ± 0.1) dB at 800 nm. Using such result together with the measured transmission, we determined the guiding losses as (0.4 ± 0.1) dB/mm and (0.5 ± 0.1) dB/mm, respectively. Such losses are equivalent to the ones reported in type I waveguides produced by the same method in commercial silicate glass (Corning 0215), being of 0.3 dB/mm also at 632.8 nm.¹⁰⁷

As previously mentioned, the L-threonine crystal was cut to satisfy the phase-matching condition for second harmonic generation at 371 nm, i.e., using a fundamental beam at 742 nm. By using the coupling setup with a 0.1 NA lens, chosen to obtain higher coupling efficiency, we obtained (23.7 ± 0.5) % of transmission and (0.56 ± 0.06) dB/mm of guiding losses for the waveguide at 742 nm. Such values are in agreement with the ones we found at 632.8 and 800 nm. In Fig. 5.7(a), it is shown the average power of the SHG guided beam (black squares) and the conversion efficiency (blue circles) at the output of the waveguide, as function of the fundamental beam average power. The inset in this figure presents the intensity profile of the guided mode at the second harmonic. It can be seen that the generated light (black squares) follows the quadratic dependence with the fundamental beam power, as expected for a second harmonic generation process. Since the conversion depends on the squared fundamental input power and crystal length, it is useful to define a normalized power conversion efficiency as¹⁰⁸:

$$\bar{\eta}_P = \frac{P_{2\omega}^\infty}{L^2(P_\omega^\infty)^2} \quad (5.1)$$

in which L correspond to the waveguide length, $P_{2\omega}^\infty$ is the peak power of the second harmonic beam and P_ω^∞ is the peak power of the fundamental beam at the output of the waveguide. From the second harmonic generation data, the normalized conversion efficiency of the cladding waveguide inscribed in L-threonine crystal was calculated to be (10.3 ± 0.4) % $(\text{MW cm}^2)^{-1}$.

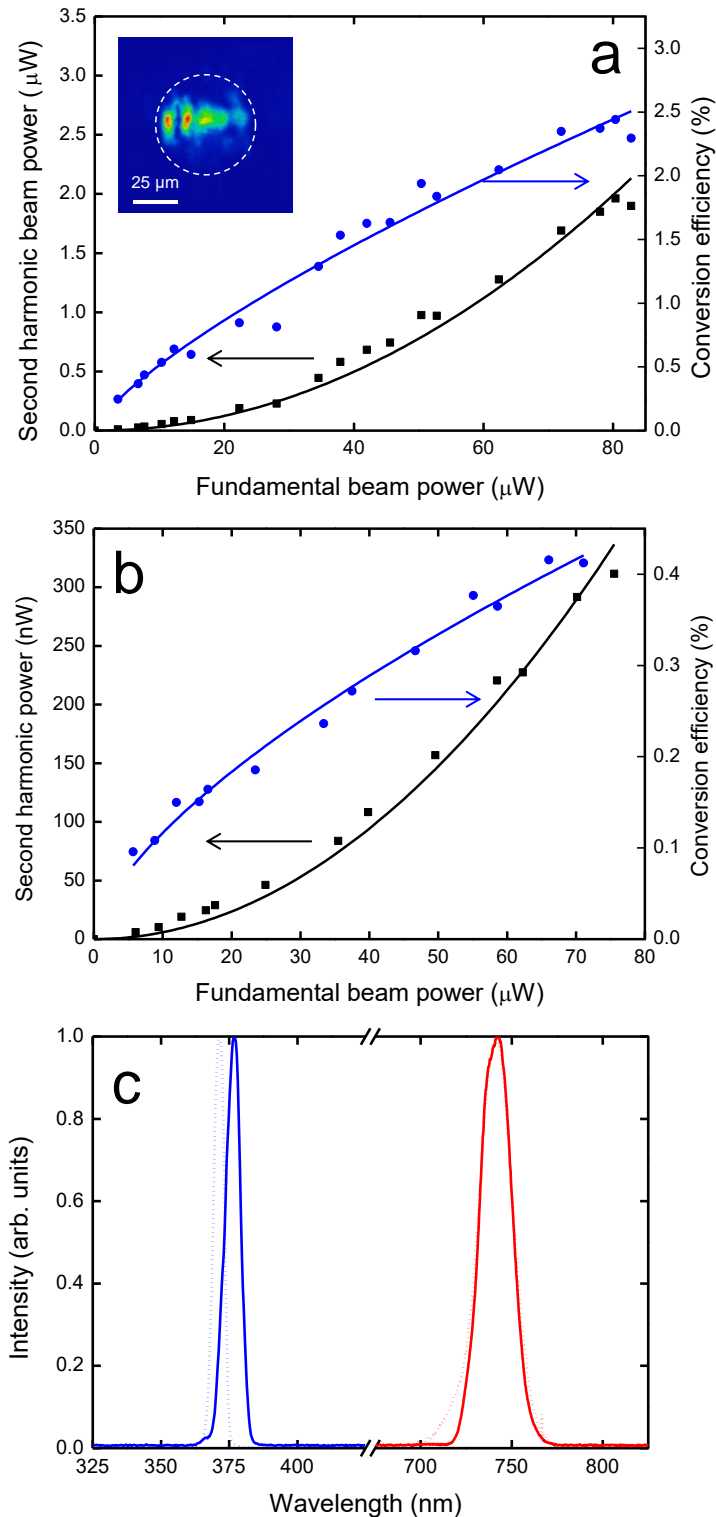


Figure 5.7 – (a) Guided second harmonic beam power (black squares) and its conversion efficiency (blue circles) as function of the fundamental beam power at the waveguide output. The inset corresponds to the mode intensity distribution of the guided second harmonic. (b) Second harmonic beam power (black squares) and its conversion efficiency (blue circles) as function of the fundamental beam power for the crystal. (c) Spectra of fundamental input (red) and second harmonic output (blue) beams in the crystal (dotted line) and guided within the waveguide (solid line).

Source: By the author.

For comparison, we also studied the SHG in the bulk L-threonine crystal at 742 nm by using a lens with a focal distance of 55 cm. Again, the expected quadratic dependence of the second harmonic power with the fundamental power was observed, as shown in Fig. 5.7(b) (black squares). The corresponding conversion efficiency as function of the fundamental beam average power is also shown in Fig. 5.7 (b) (blue circles). Figure 5.7 (c) displays the spectra of the fundamental input beam (red) and second harmonic output beam (blue) for the case of the cladding waveguide (solid lines) and the L-threonine crystal (dotted lines). It can be seen that both input beams are centered at 742 nm, while the second harmonic generated by the crystal is at 371 nm and the one generated by the waveguide is at 377 nm.

Since the SHG is an intensity dependent process, a proper comparison should take into account the area of the beam, thus, it is convenient to define a normalized intensity conversion efficiency as:

$$\bar{\eta}_I = \frac{I_{2\omega}^\infty}{L^2(I_\omega^\infty)^2} \quad (5.2)$$

in which I_ω^∞ and $I_{2\omega}^\infty$ are the peak intensity of the fundamental and second harmonic beam, respectively. Therefore, considering the mode area obtained from the guided intensity distribution profile (for the waveguide) and the beam area (for the bulk crystal) we found $(0.16 \pm 0.02) \% (\text{GW})^{-1}$ and $(0.04 \pm 0.01) \% (\text{GW})^{-1}$ for the cladding waveguide and the bulk crystal, respectively. As one can note, the inscribed cladding waveguides present approximately 4 times higher normalized intensity conversion efficiency than the crystal itself. Such increase may be understood by considering the influence of the waveguide dispersion contribution to the phase matching condition. The wave vector \vec{k} for a propagating wave in a low numerical aperture waveguide can be described by $\vec{k} \cong \vec{k}_{mat} - \vec{k}_{mode}$,¹⁰⁹ which takes into account both, material \vec{k}_{mat} and modal \vec{k}_{mode} dispersion terms. Therefore, compared to the material only scenario, the total phase matching conditions is altered to $\Delta\vec{k} \cong \Delta\vec{k}_{mat} - \Delta\vec{k}_{mode}$ and such influence is evidenced in a small shift in the second harmonic spectrum allowed by the broad bandwidth of the input pulse. Further analysis on the impact of the wave-guiding on the phase matching is out of the scope of this work due to the complexity of the multimode being guided at both fundamental and harmonic wavelengths.

5.4 Partial conclusion

We reported the production of cladding waveguides in organic crystals using fs-laser inscription and its application to guided broadband second harmonic generation of UV femtosecond pulses. A circular cross-section cladding waveguide, composed of 20 parallel tracks was designed 100 μm beneath the surface of an L-threonine monocrystal, using 50-fs pulses at optimal energy of 14 nJ. Through waveguide transmission analyses as function of the numerical aperture (NA) of the coupling lens, we obtained that the NA of such waveguide is smaller than 0.1, corresponding to a refractive index change below 2×10^{-3} . Coupling and propagation losses at visible/IR region are on the order of 4 dB and 0.5 dB/mm, respectively. Finally, and more interestingly, we achieved broadband second harmonic generation of UV femtosecond pulses (377 nm) with power conversion efficiency of $(10.3 \pm 0.4) \% (\text{MW cm}^2)^{-1}$ and higher intensity conversion efficiency than by means of the free-space focusing at L-threonine monocrystal. Such result shows the potential of inscription of waveguides on nonlinear organic materials aiming the enhancement of its nonlinear optical effects through the extension of nonlinear interaction region via the optical field tight-confinement.

6 CONCLUSIONS AND PERSPECTIVES

In this dissertation, we have studied the optical nonlinearities in bulk and in femtosecond laser inscribed waveguides in Gorilla Glass and L-threonine organic crystals. Throughout our investigations, nonlinear optical properties were measured applying different techniques depending on the particular order of the nonlinearity and distinct types of written waveguides, in order to develop nonlinear devices that generate and guide white-light continuum and second harmonic. This chapter summarizes our results and findings.

In the first part, a set of experiments were carried out in Gorilla Glass. Measurements of its third-order nonlinearities in the spectral grange from the visible to the near infrared region revealed a constant nonlinear refractive index of $(3.3 \pm 0.6) \times 10^{-20} \text{ m}^2/\text{W}$ and an ultrafast response time. Regarding the femtosecond laser processing of Gorilla Glass, it was shown to be wavelength independent. Waveguides inscribed with pulse energy lower than the ablation threshold were shown to operate in the single mode regime. The determined propagation losses, on the order of $(0.3 \pm 0.01) \text{ dB/mm}$, put the waveguides inscribed in this work in competition with other laser written waveguides in glassy materials. When ultrashort pulses were coupled into the waveguide, their guided output spectrum presented white-continuum generation (450 – 800 nm) due to self-phase modulation and stimulated Raman scattering, since the pump is in the normal dispersion regime. In addition to the huge popularity and excellent mechanical properties of Gorilla Glass, our results draw more attention to it as a good candidate for an integrated nonlinear optical platform.

In the second part, cladding waveguides were inscribed in amino acid L-threonine organic crystal. Such structure was chosen because desired original material properties are kept unaltered in its core region during femtosecond laser writing, allowing light guidance through an unmodified material. The inscribed waveguides presented as linear features multi-mode propagation and attenuation on the order of 0.5 dB/mm. Regarding its nonlinear characteristics, ultra-violet second harmonic generation and guidance was demonstrated with normalized power conversion efficiency of $(10.3 \pm 0.4) \% (\text{MW cm}^2)^{-1}$. Also, its normalized intensity conversion efficiency was found to be four times higher than the L-threonine crystal alone. Such improvement is addressed to the contribution of the waveguide dispersion in the material dispersion relation, altering the phase-matching condition required in

nonlinear parametric conversion phenomena. Another indication of that is the shifted second harmonic spectrum observed at the waveguides output. Overall, second harmonic generation is an important nonlinear phenomenon that has been quickly incorporated into waveguide devices; we have performed it in an organic matrix and pushed it into the UV spectral region.

The studies described in this dissertation reinforce the potential and versatility of femtosecond laser processing as a tool for the development of several photonic devices in different materials. Besides what we have done here, we look forward to producing more complex waveguiding structures. For example, Mach-Zehnder interferometer and beam splitters. Other application that can be addressed using ultrashort laser micromachining is the production of color centers in diamond which can produce negatively charged Nitrogen-vacancy centers, which can act as optical qubits for room temperature quantum information processing.

REFERENCES

- 1 MAIMAN, T. H. Stimulated optical emission in ruby. **Journal of the Optical Society of America**, v. 50, n. 11, p. 1134-1134, 1960.
- 2 FRANKEN, P. A. et al. Generation of optical harmonics. **Physical Review Letters**, v. 7, n. 4, p. 118, 1961.
- 3 KAISER, W.; GARRETT, C. G. B. 2-photon excitation in $\text{CaF}_2 - \text{Eu}^{2+}$. **Physical Review Letters**, v. 7, n. 6, p. 229, 1961.
- 4 LIU, X.; DU, D.; MOUROU, G. Laser ablation and micromachining with ultrashort laser pulses. **IEEE Journal of Quantum Electronics**, v. 33, n. 10, p. 1706-1716, 1997.
- 5 CHICHKOV, B. N. et al. Femtosecond, picosecond and nanosecond laser ablation of solids. **Applied Physics A: materials science & processing**, v. 63, n. 2, p. 109-115, 1996.
- 6 HAIGHT, R. et al. High resolution material ablation and deposition with femtosecond lasers and applications to photomask repair. **Journal of Modern Optics**, v. 51, n. 16-18, p. 2781-2796, 2004.
- 7 PRONKO, P. P. et al. Machining of submicron holes using a femtosecond laser at 800-nm. **Optics Communications**, v. 114, n. 1-2, p. 106-110, 1995.
- 8 WLODARCZYK, K. L. et al. Laser microsculpting for the generation of robust diffractive security markings on the surface of metals. **Journal of Materials Processing Technology**, v. 222, p. 206-218, 2015. doi.org/10.1016/j.jmatprotec.2015.03.001.
- 9 ZHAO, Q. Z. et al. Direct writing computer-generated holograms on metal film by an infrared femtosecond laser. **Optics Express**, v. 13, n. 6, p. 2089-2092, 2005.
- 10 JENNESS, N. J. et al. A versatile diffractive maskless lithography for single-shot and serial microfabrication. **Optics Express**, v. 18, n. 11, p. 11754-11762, 2010.
- 11 STROHABER, J.; SCARBOROUGH, T. D.; UITERWAAL, C. Ultrashort intense-field optical vortices produced with laser-etched mirrors. **Applied Optics**, v. 46, n. 36, p. 8583-8590, 2007.

12 MANZOLI, A. et al. Femtosecond laser ablation of gold interdigitated electrodes for electronic tongues. **Optics and Laser Technology**, v. 69, p. 148-153, 2015. doi.org/10.1016/j.optlastec.2014.12.026.

13 PERRIERE, J. et al. Nanoparticle formation by femtosecond laser ablation. **Journal of Physics D : applied physics**, v. 40, n. 22, p. 7069-7076, 2007.

14 VOROBYEV, A. Y.; GUO, C. L. Multifunctional surfaces produced by femtosecond laser pulses. **Journal of Applied Physics**, v. 117, n. 3, 2015. doi.org/10.1063/1.4905616.

15 TULL, B. R. et al. Silicon surface morphologies after femtosecond laser irradiation. **MRS Bulletin**, v. 31, n. 8, p. 626-633, 2006.

16 HER, T. H. et al. Microstructuring of silicon with femtosecond laser pulses. **Applied Physics Letters**, v. 73, n. 12, p. 1673-1675, 1998.

17 ALMEIDA, G. F. B. et al. Laser induced periodic surface structuring on Si by temporal shaped femtosecond pulses. **Optics Express**, v. 23, n. 21, p. 27597-27605, 2015.

18 WU, C. et al. Near-unity below-band-gap absorption by microstructured silicon. **Applied Physics Letters**, v. 78, n. 13, p. 1850-1852, 2001.

19 ALMEIDA, G. F. B. et al. Surface morphology and structural modification induced by femtosecond pulses in hydrogenated amorphous silicon films. **Journal of Nanoscience and Nanotechnology**, v. 15, n. 3, p. 2495-2500, 2015.

20 BONSE, J. et al. Femtosecond laser ablation of silicon-modification thresholds and morphology. **Applied Physics A : materials science & processing**, v. 74, n. 1, p. 19-25, 2002.

21 GATTASS, R. R.; MAZUR, E. Femtosecond laser micromachining in transparent materials. **Nature Photonics**, v. 2, n. 4, p. 219-225, 2008.

22 GLEZER, E. N. et al. Three-dimensional optical storage inside transparent materials. **Optics Letters**, v. 21, n. 24, p. 2023-2025, 1996.

23 MASELLI, V. et al. Fabrication of long microchannels with circular cross section using astigmatically shaped femtosecond laser pulses and chemical etching. **Applied Physics Letters**, v. 88, n. 19, 2006. doi:10.1063/1.2203335.

24 LIAO, Y. et al. Rapid prototyping of three-dimensional microfluidic mixers in glass by femtosecond laser direct writing. **Lab on a Chip**, v. 12, n. 4, p. 746-749, 2012.

25 MARUO, S.; NAKAMURA, O.; KAWATA, S. Three-dimensional microfabrication with two-photon-absorbed photopolymerization. **Optics Letters**, v. 22, n. 2, p. 132-134, 1997.

26 TRIBUZI, V. et al. Birefringent microstructures fabricated by two-photon polymerization containing an azopolymer. **Optical Materials Express**, v. 3, n. 1, p. 21-26, 2013.

27 STRAUB, M.; GU, M. Near-infrared photonic crystals with higher-order bandgaps generated by two-photon photopolymerization. **Optics Letters**, v. 27, n. 20, p. 1824-1826, 2002.

28 GUO, R. et al. Micro lens fabrication by means of femtosecond two photon photopolymerization. **Optics Express**, v. 14, n. 2, p. 810-816, 2006.

29 DORAISWAMY, A. et al. Fabrication of microneedles using two photon polymerization for transdermal delivery of nanomaterials. **Journal of Nanoscience and Nanotechnology**, v. 10, n. 10, p. 6305-6312, 2010.

30 AVILA, O. I. et al. Fabrication of microenvironments with different geometrical features for cell growth studies. **Journal of Laser Micro Nanoengineering**, v. 9, n. 3, p. 248-251, 2014.

31 OTUKA, A. J. G. et al. Direct laser writing by two-photon polymerization as a tool for developing microenvironments for evaluation of bacterial growth. **Materials Science & Engineering C: materials for biological applications**, v. 35, p. 185-189, 2014. doi.org/10.1016/j.msec.2013.11.005.

32 OTUKA, A. J. G. et al. Emission features of microstructures fabricated by two-photon polymerization containing three organic dyes. **Optical Materials Express**, v. 2, n. 12, p. 1803-1808, 2012.

33 TOMAZIO, N. B. et al. Femtosecond laser fabrication of high-q whispering gallery mode microresonators via two-photon polymerization. **Journal of Polymer Science B: polymer physics**, v. 55, n. 7, p. 569-574, 2017.

34 TOMAZIO, N. B.; DE BONI, L.; MENDONÇA, C. R. Low threshold Rhodamine-doped whispering gallery mode microlasers fabricated by direct laser writing. **Scientific Reports**, v. 7, 2017. doi.org/ 10.1038/s41598-017-09293-z.

35 MARUO, S.; INOUE, H. Optically driven micropump produced by three-dimensional two-photon microfabrication. **Applied Physics Letters**, v. 89, n. 14, 2006. doi.org/10.1063/1.2358820.

36 DAVIS, K. M. et al. Writing waveguides in glass with a femtosecond laser. **Optics Letters**, v. 21, n. 21, p. 1729-1731, 1996.

37 CHEN, F.; DE ALDANA, J. R. V. Optical waveguides in crystalline dielectric materials produced by femtosecond-laser micromachining. **Laser & Photonics Reviews**, v. 8, n. 2, p. 251-275, 2014.

38 NEJADMALAYERI, A. H. et al. Inscription of optical waveguides in crystalline silicon by mid-infrared femtosecond laser pulses. **Optics Letters**, v. 30, n. 9, p. 964-966, 2005.

39 NOLTE, S. et al. Femtosecond waveguide writing: a new avenue to three-dimensional integrated optics. **Applied Physics A: materials science & processing**, v. 77, n. 1, p. 109-111, 2003.

40 EATON, S. M. et al. Telecom-band directional coupler written with femtosecond fiber laser. **IEEE Photonics Technology Letters**, v. 18, n. 17-20, p. 2174-2176, 2006.

41 KOWALEVICZ, A. M. et al. Three-dimensional photonic devices fabricated in glass by use of a femtosecond laser oscillator. **Optics Letters**, v. 30, n. 9, p. 1060-1062, 2005.

42 CORRIELLI, G. et al. Rotated waveplates in integrated waveguide optics. **Nature Communications**, v. 5, 2014. doi.org/10.1038/ncomms5249

43 CRESPI, A. et al. Three-dimensional Mach-Zehnder interferometer in a microfluidic chip for spatially-resolved label-free detection. **Lab on a Chip**, v. 10, n. 9, p. 1167-1173, 2010.

44 ZHANG, H. B.; EATON, S. M.; HERMAN, P. R. Single-step writing of Bragg grating waveguides in fused silica with an externally modulated femtosecond fiber laser. **Optics Letters**, v. 32, n. 17, p. 2559-2561, 2007.

45 MARSHALL, G. D.; AMS, M.; WITHFORD, M. J. Direct laser written waveguide-Bragg gratings in bulk fused silica. **Optics Letters**, v. 31, n. 18, p. 2690-2691, 2006.

46 LAPOINTE, J. et al. Making smart phones smarter with photonics. **Optics Express**, v. 22, n. 13, p. 15473-15483, 2014.

47 YU, A. M. et al. Efficient second harmonic generation in a KDP crystal pumped with picosecond YAG:Nd³⁺ laser pulses of 0.5 Hz repetition frequency. **Soviet Journal of Quantum Electronics**, v. 8, n. 3, p. 386, 1978.

48 DRISCOLL, T. A. et al. Efficient second-harmonic generation in KTP crystals. **Journal of the Optical Society of America B**, v. 3, n. 5, p. 683-686, 1986.

49 LIU, H.; YAO, J.; PURI, A. Second and third harmonic generation in BBO by femtosecond Ti: sapphire laser pulses. **Optics Communications**, v. 109, n. 1, p. 139-144, 1994.

50 RODRIGUES, J. J. et al. Optical properties of L-threonine crystals. **Optical Materials**, v. 22, n. 3, p. 235-240, 2003.

51 GRIFFITHS, D. J. **Introduction to electrodynamics**. New York: Prentice Hall, 1999.

52 JACKSON, J. D. **Classical electrodynamics**. New York: Wiley, 1975.

53 BOYD, R. W. Wave-equation description of nonlinear optical interactions. In: _____(Ed.). **Nonlinear optics**. 3rd ed. Burlington: Academic Press, 2008. cap. 2, p.69-133.

54 BOYD, R. W. The intensity-dependent refractive index. In: _____(Ed.). **Nonlinear optics**. 3rd ed. Burlington: Academic Press, 2008. cap. 4.p.207-252.

55 MILAM, D. Review and assessment of measured values of the nonlinear refractive-index coefficient of fused silica. **Applied Optics**, v. 37, n. 3, p. 546-550, 1998.

56 YARIV, A. **Quantum electronics**. New York: Wiley, 1989.

57 RAPOPORT, W. R.; KHATTAK, C. P. Titanium sapphire laser characteristics. **Applied Optics**, v. 27, n. 13, p. 2677-2684, 1988.

58 FOWLES, G. R. **Introduction to modern optics**. New York: Dover Publications, 1975.

59 STRICKLAND, D.; MOUROU, G. Compression of amplified chirped optical pulses. **Optics Communications**, v. 56, n. 3, p. 219-221, 1985.

60 ANISIMOV, S. I.; KAPELIOVICH, B. L.; PERELMAN, T. L. Electron-emission from surface of metals induced by ultrashort laser pulses. **Zhurnal Eksperimentalnoi i Teoreticheskoi Fiziki**, v. 66, n. 2, p. 776-781, 1974.

61 KELDYSH, L. Ionization in the field of a strong electromagnetic wave. **Soviet Physics JETP**, v. 20, n. 5, p. 1307-1314, 1965.

62 WEGENER, M. **Extreme nonlinear optics: an introduction**. Berlin: Springer Verlag, 2006.

63 ILKOV, F. A.; DECKER, J. E.; CHIN, S. L. Ionization of atoms in the tunneling regime with experimental-evidence using hg atoms. **Journal of Physics B: atomic molecular and optical physics**, v. 25, n. 19, p. 4005-4020, 1992.

64 STUART, B. C. et al. Nanosecond-to-femtosecond laser-induced breakdown in dielectrics. **Physical Review B**, v. 53, n. 4, p. 1749-1761, 1996.

65 SCHAFFER, C. B.; BRODEUR, A.; MAZUR, E. Laser-induced breakdown and damage in bulk transparent materials induced by tightly focused femtosecond laser pulses. **Measurement Science and Technology**, v. 12, n. 11, p. 1784-1794, 2001.

66 KONIG, J.; NOLTE, S.; TUNNERMANN, A. Plasma evolution during metal ablation with ultrashort laser pulses. **Optics Express**, v. 13, n. 26, p. 10597-10607, 2005.

67 FLOREA, C.; WINICK, K. A. Fabrication and characterization of photonic devices directly written in glass using femtosecond laser pulses. **Journal of Lightwave Technology**, v. 21, n. 1, p. 246-253, 2003.

68 MIURA, K. et al. Photowritten optical waveguides in various glasses with ultrashort pulse laser. **Applied Physics Letters**, v. 71, n. 23, p. 3329-3331, 1997.

69 CHAN, J. W. et al. Structural changes in fused silica after exposure to focused femtosecond laser pulses. **Optics Letters**, v. 26, n. 21, p. 1726-1728, 2001.

70 CHAN, J. W. et al. Waveguide fabrication in phosphate glasses using femtosecond laser pulses. **Applied Physics Letters**, v. 82, n. 15, p. 2371-2373, 2003.

71 CHAN, J. W. et al. Modification of the fused silica glass network associated with waveguide fabrication using femtosecond laser pulses. **Applied Physics A: materials science & processing**, v. 76, n. 3, p. 367-372, 2003.

72 GLEZER, E. N.; MAZUR, E. Ultrafast-laser driven micro-explosions in transparent materials. **Applied Physics Letters**, v. 71, n. 7, p. 882-884, 1997.

73 HASHIMOTO, T.; JUODKAZIS, S.; MISAWA, H. Void formation in glasses. **New Journal of Physics**, v. 9, 2007. doi.org/10.1088/1367-2630/9/8/253

74 GORELIK, T. et al. Transmission electron microscopy studies of femtosecond laser induced modifications in quartz. **Applied Physics A: materials science & processing**, v. 76, n. 3, p. 309-311, 2003.

75 LIU, J. M. Simple technique for measurements of pulsed gaussian-beam spot sizes. **Optics Letters**, v. 7, n. 5, p. 196-198, 1982.

76 EATON, S. M.; ZHANG, H. B.; HERMAN, P. R. Heat accumulation effects in femtosecond laser-written waveguides with variable repetition rate. **Optics Express**, v. 13, n. 12, p. 4708-4716, 2005.

77 SALEH, B. E. A.; TEICH, M. C. **Fundamentals of photonics**. New Jersey: Wiley, 2007.

78 AGRAWAL, G. P. **Nonlinear fiber optics**. Oxford: Academic Press, 2007.

79 FERREIRA, M. F. **Nonlinear effects in optical fibers**. New Jersey: Wiley, 2011.

80 DUDLEY, J. M.; GENTY, G.; COEN, S. Supercontinuum generation in photonic crystal fiber. **Reviews of Modern Physics**, v. 78, n. 4, p. 1135-1184, 2006.

81 BOYD, R. W. Stimulated raman scattering and stimulated rayleigh-wing scattering. In: _____. **Nonlinear optics**. 3rd ed. Burlington: Academic Press, 2008. cap. 10, p.473-509.

82 ALMEIDA, J. M. P. et al. Third-order nonlinear spectra and optical limiting of lead oxifluoroborate glasses. **Optics Express**, v. 19, n. 18, p. 17220-17225, 2011.

83 MANZANI, D. et al. Nonlinear optical properties of tungsten lead-pyrophosphate glasses containing metallic copper nanoparticles. **Plasmonics**, v. 8, n. 4, p. 1667-1674, 2013.

84 BLOMER, D. et al. Nonlinear refractive index of fs-laser-written waveguides in fused silica. **Optics Express**, v. 14, n. 6, p. 2151-2157, 2006.

85 NAKAMURA, S. et al. Femtosecond laser direct writing of optical waveguides in silicone film. **Journal of Laser Micro Nanoengineering**, v. 2, n. 3, p. 189-193, 2007.

86 OSELLAME, R.; CERULLO, G.; RAMPONI, R. **Femtosecond laser micromachining**: photonic and microfluidic devices in transparent materials. Berlin: Springer, 2012.

87 OSELLAME, R. et al. Optical waveguide writing with a diode-pumped femtosecond oscillator. **Optics Letters**, v. 29, n. 16, p. 1900-1902, 2004.

88 ALMEIDA, G. F. B. et al. Third-order optical nonlinearities in bulk and fs-laser inscribed waveguides in strengthened alkali aluminosilicate glass. **Laser Physics**, v. 28, n. 1, p.015401,2018.

89 AGRAWAL, G. Highly nonlinear fibers. In: _____. **Nonlinear fiber optics** 5th ed. Boston: Academic Press, 2013. cap. 11, p.457-496.

90 GREHN, M. et al. Nonlinear absorption and refraction of binary and ternary alkaline and alkaline earth silicate glasses. **Optical Materials Express**, v. 3, n. 12, p. 2132-2140, 2013.

91 GROSSMANN, D. et al. Transverse pump-probe microscopy of moving breakdown, filamentation and self-organized absorption in alkali aluminosilicate glass using ultrashort pulse laser. **Optics Express**, v. 24, n. 20, p. 23221-23231, 2016.

92 SALIMINIA, A. et al. Writing optical waveguides in fused silica using 1 kHz femtosecond infrared pulses. **Journal of Applied Physics**, v. 93, n. 7, p. 3724-3728, 2003.

93 OSELLAME, R. et al. Femtosecond writing of active optical waveguides with astigmatically shaped beams. **Journal of the Optical Society of America B: optical physics**, v. 20, n. 7, p. 1559-1567, 2003.

94 DUMAIS, P. et al. Enhanced self-phase modulation in tapered fibers. **Optics Letters**, v. 18, n. 23, p. 1996-1998, 1993.

95 DUDLEY, J. M. et al. Supercontinuum generation in air-silica microstructured fibers with nanosecond and femtosecond pulse pumping. **Journal of the Optical Society of America B: optical physics**, v. 19, n. 4, p. 765-771, 2002.

96 GATTASS, R. R. et al. Supercontinuum generation in submicrometer diameter silica fibers. **Optics Express**, v. 14, n. 20, p. 9408-9414, 2006.

97 GLOGE, D. Weakly guiding fibers. **Applied Optics**, v. 10, n. 10, p. 2252, 1971.

98 MISOGUTI, L. et al. Optical properties of L-alanine organic crystals. **Optical Materials**, v. 6, n. 3, p. 147-152, 1996.

99 PAN, F. et al. A highly efficient organic second-order nonlinear optical crystal based on a donor-acceptor substituted 4-nitrophenylhydrazone. **Applied Physics Letters**, v. 71, n. 15, p. 2064-2066, 1997.

100 JIA, Y. et al. Second harmonic generation of violet light in femtosecond-laser-inscribed BiB_3O_6 cladding waveguides. **Optical Materials Express**, v. 3, n. 9, p. 1279-1284, 2013.

101 YUECHEN, J. et al. Femtosecond-laser-inscribed BiB_3O_6 nonlinear cladding waveguide for second-harmonic generation. **Applied Physics Express**, v. 5, n. 7, p. 072701, 2012.

102 LIU, H. L. et al. Femtosecond laser inscribed cladding waveguides in Nd:YAG ceramics: fabrication, fluorescence imaging and laser performance. **Optics Express**, v. 20, n. 17, p. 18620-18629, 2012.

103 SHOEMAKER, D. P. et al. The crystal structure of L_s -threonine¹. **Journal of the American Chemical Society**, v. 72, n. 6, p. 2328-2349, 1950.

104 CLARK, R. L.; KRC, J. Crystallographic data. 59 L_3 -Threonine (Threo- α -amino- β -hydroxy-n-butyric Acid). **Analytical Chemistry**, v. 24, n. 8, p. 1378-1379, 1952.

105 NIE, W. J. et al. Efficient second harmonic generation in 3D nonlinear optical-lattice-like cladding waveguide splitters by femtosecond laser inscription. **Scientific Reports**, v. 6, 2016. doi.org/ 10.1038/srep22310.

106 DONG, N.; CHEN, F.; VÁZQUEZ DE ALDANA, J. R. Efficient second harmonic generation by birefringent phase matching in femtosecond-laser-inscribed KTP cladding waveguides. **Physica Status Solidi: rapid research letters**, v. 6, n. 7, p. 306-308, 2012.

107 TONG, L. M. et al. Optical loss measurements in femtosecond laser written waveguides in glass. **Optics Communications**, v. 259, n. 2, p. 626-630, 2006.

108 PLISKA, T. et al. Linear and nonlinear optical properties of KNbO₃ ridge waveguides. **Journal of Applied Physics**, v. 84, n. 3, p. 1186-1195, 1998.

109 MARCATILI, E. A. J.; SCHMELTZER, R. A. Hollow metallic and dielectric waveguides for long distance optical transmission and lasers. **The Bell System Technical Journal**, v. 43, n. 4, p. 1783-1809, 1964.

APENDIX A – List of publications and conference presentations

- Published:

Third-order optical nonlinearities in bulk and fs-laser inscribed waveguides in strengthened alkali aluminosilicate glass

ALMEIDA, G. F. B.; Almeida, J. M. P.; Martins, R. J.; De Boni, L.; Arnold, C. B.; Mendonca, C. R.

Laser Physics, 28, 015401 (2018)

Femtosecond laser micromachining of polylactic acid/graphene composites for designing interdigitated microelectrodes for sensor applications

Paula, J. T.; Gaál, J.; **ALMEIDA, G. F. B.**; Andrade, M. B.; Facure, M. H. M.; Corrêa, D. S.; Riul, Antônio; Rodrigues, V.; Mendonca, C. R.

Optics & Laser Technology, 101, 74-79 (2018)

Fs-laser direct writing for spatially localized synthesis of PPV

Avila, O. A.; Almeida, J. M. P.; Henrique, F. R.; Fonseca, R. D.; **ALMEIDA, G. F. B.**; Balogh, D. T.; Medonça, C. R.

Journal of Materials Chemistry C, 5, 3579-3584 (2017)

Femtosecond laser writing of high-Q whispering gallery mode microresonators via two-photon polymerization

Tomazio, N. B.; Otuka, A. J. G.; **ALMEIDA, G. F. B.**; Roselló-Mechó, X.; Andrés, M. V.; Mendonça, C. R.

Journal of Polymer Science, Part B: Polymer Physics (2017)

Ultrafast laser pulses for structuring materials at micro/nano scale: from waveguides to superhydrophobic surfaces

Correa, D. S.; Almeida, J. M. P.; **ALMEIDA, G. F. B.**; Cardoso, M. R. De Boni, L. Mendonça, C. R.

Photonics, 4 (1), 8 (2017)

Architecture of lead oxide microcrystals in glass: a laser and etching based method

Almeida, J. M. P.; **ALMEIDA, G. F. B.**; A. C. Hernandez, A. C.; Mendonça, C. R.
CrystEngComm, 2016, 18, 5959-5964 (2016)

Laser induced periodic surface structuring on Si by temporal shaped femtosecond pulses

ALMEIDA, G. F. B.; Martins, R. J.; Otuka, A. J. G.; Siqueira, J. P.; Mendonca, C. R.
Optics Express, 23, 27597-27605 (2015)

Single-walled Carbon nanotubes functionalizes with carboxylic acid for fabricating polymeric composite microstructures

Otuka, A. J. G.; Tribuzi, V.; Cardoso, M; R.; **ALMEIDA, G. F. B.**; Zanatta, A. R.; Correa, D. S.; Menconca, C. R.
Journal of Nanoscience and Nanotechnology, 15, 9797-9801 (2015)

Nonlinear optical properties and femtosecond laser micromachining of special glasses

Almeida, J. M. P.; **ALMEIDA, G. F. B.**; De Boni, L; Mendonca, C. R.
Journal of Brazilian Chemical Society, 26, 2418-2429 (2015)

A survey on multiphoton lithography for fabricating optical microdevices

Tribuzi, V.; Otuka, A. J. G.; **ALMEIDA, G. F. B.**; Correa, D. S.; Mendonca, C. R.
Display and Imaging, 2, pp. 29–47 (2015)

Femtosecond laser ablation of gold interdigitated electrodes for electronic tongues

Manzoli, A.; **ALMEIDA, G. F. B.**; Filho, J. A.; Mattoso, L. H. C.; Ruil Jr., A.; Mendonca, C. R.; Correa, D. S.
Optics & Laser Technology, 69, 148–153 (2015)

Surface morphology and structural modification induced by femtosecond pulses in hydrogenated amorphous silicon films

ALMEIDA, G. F. B.; Cardoso, M. R.; Aoki, P. H. B.; Lima, J. J. D.; Da Costa, L. F.; Rodrigues, C. A.; Constantino, C. J. L.; Mendonca, M. R.
Journal of Nanoscience and Nanotechnology, 15, 2495-2500 (2015)

Microfabrication of electroluminescent polymer for devices construction

Estevam-Alves, R.; Ferreira, P. H. D.; **ALMEIDA, G. F. B.**; Souza, W. S.; Mendonca, C. R.

Applied Surface Science, 314, 633-637 (2014)

- Submitted:

Nonlinear optical waveguides inscribed by fs-laser in organic crystal for broadband second harmonic generation of UV pulses

ALMEIDA, G. F. B.; Martins, R. J.; Siqueira, J. P.; Almeida, J. M. P.; Rodrigues Jr., J. J.; Mendonça, C. R.

Measurements of refractive index profile of waveguide in glasses using Defocusing Microscopy

Lages, E; Cardoso, W. R.; **ALMEIDA, G. F. B.**; Mendonça, C. R.; Agero, U.; Pádua, S.

- Selected conference presentations:

Femtosecond laser writing of cladding waveguides in L-threonine crystals

ALMEIDA, G. F. B.; Martins, R. J.; Siqueira, J. P.; Almeida, J. M. P.; Rodrigues Jr., J. J.; Mendonça, C. R.

10th International Conference on Nanophotonics 2017, Recife, Pernambuco – Brazil

Fabrication of waveguides in Gorilla® Glass with fs-pulses and its nonlinear features

ALMEIDA, G. F. B.; Almeida, J. M. P.; Martins, R. J.; De Boni, L.; Arnold, C. B.; Mendonca, C. R.

SPIE Photonics West 2017, San Francisco, California – United States

Ultrafast laser inscribed waveguides in Gorilla Glass and its nonlinearities

ALMEIDA, G. F. B.; Almeida, J. M. P.; Martins, R. J.; De Boni, L; Arnold, C. B.; Mendonça, C. R.

São Paulo School of Science on Nanophotonics and XV Jorge Andre Swieca School on Nonlinear and Quantum Optics 2016, Campinas, São Paulo – Brazil

Exploring silicon vibration resonance in micromachining applying temporal shaped femtosecond laser pulses

ALMEIDA, G. F. B.; Martins, R. J.; Otuka, A. J. G.; Mendonca, C. R.

The European Conference on Laser and Electro-Optics (OSA CLEO-Europe) 2015, Munich – Germany

Silicon micromachining using femtosecond shaped laser pulses

ALMEIDA, G. F. B.; Martins, R. J.; Otuka, A. J. G.; Mendonca, C. R.

XXXVIII Encontro Nacional de Física da Matéria Condensada 2015, Foz do Iguaçu, Paraná – Brazil